Nanoscale Advances

ROYAL SOCIETY OF CHEMISTRY

REVIEW

View Article Online
View Journal | View Issue

Check for updates

Cite this: *Nanoscale Adv.*, 2020, **2**, 583

Nanostructured metal chalcogenides confined in hollow structures for promoting energy storage

Ying Liu, Zhiwen Che, Xuyun Lu, Xiaosi Zhou, Min Han, Jianchun Bao * and Zhihui Dai *

Received 30th November 2019
Accepted 25th December 2019

DOI: 10.1039/c9na00753a

rsc.li/nanoscale-advances

The engineering of progressive nanostructures with subtle construction and abundant active sites is a key factor for the advance of highly efficient energy storage devices. Nanostructured metal chalcogenides confined in hollow structures possess abundant electroactive sites, more ions and electron pathways, and high local conductivity, as well as large interior free space in a quasi-closed structure, thus showing promising prospects for boosting energy-related applications. This review focuses on the most recent progress in the creation of diverse confined hollow metal chalcogenides (CHMCs), and their electrochemical applications. Particularly, by highlighting certain typical examples from these studies, a deep understanding of the formation mechanism of confined hollow structures and the decisive role of microstructure engineering in related performances are discussed and analyzed, aiming at prompting the nanoscale engineering and conceptual design of some advanced confined metal chalcogenide nanostructures. This will appeal to not only the chemistry-, energy-, and materials-related fields, but also environmental protection and nanotechnology, thus opening up new opportunities for applications of CHMCs in various fields, such as catalysis, adsorption and separation, and energy conversion and storage.

Introduction

Nanostructured metal chalcogenides (MCs) have drawn considerable attention during the past few decades owing to their rich redox chemistry, diverse crystal structures and high electrochemical activity.[1–3] These virtues lead them to great achievements in energy storage systems, including lithium-ion batteries (LIBs), lithium–sulfur (Li–S) batteries, sodium-ion batteries (SIBs), supercapacitors, *etc.*[4–8] Particularly, compared with the traditional intercalated $LiMO_2$ cathodes (M = Mn, Ni, Co or their mixtures) of LIBs, MCs usually possess ameliorative electrochemical reversibility originating from their faster charge transfer kinetics, and higher theoretical specific capacities when used as electrode materials for batteries.[9] For instance, FeS_2 has a theoretical specific capacity of 894 mA h g^{-1} and MoS_2 demonstrates a theoretical specific capacity of 670

Jiangsu Collaborative Innovation Center of Biomedical Functional Materials, School of Chemistry and Materials Science, Nanjing Normal University, Nanjing 210023, P. R. China. E-mail: baojianchun@njnu.edu.cn; daizhihuii@njnu.edu.cn

Ying Liu is a doctoral student of Nanjing Normal University, and is under joint supervision currently at the Institute of Chemistry, Chinese Academy of Sciences (CAS). She received her Bachelor of Science (BS) from Anhui University of Science and Technology, China in 2015. Her research interests lie in the design and synthesis of some special heterogeneous nanostructures for electrocatalytic, energy storage and photoelectric sensing applications. Relevant studies have been published in J. Am. Chem. Soc., Adv. Mater., J. Mater. Chem. A, Chem. Commun., and so on.

Zhihui Dai was awarded the China National Fund for Distinguished Young Scientists, is a Changjiang scholar Distinguished Professor, received her PhD degree from Nanjing University in 2004 and now is a professor at Nanjing Normal University. Her research interests include functional nanomaterials, biochemical and electrochemical analysis and biosensors. She has published over 130 papers in journals such as J. Am. Chem. Soc., Angew. Chem., Int. Ed., Nat. Commun., Adv. Mater., ACS Nano, Anal. Chem., and Chem. Commun. She has over 4000 citations.

Open Access Article. Published on 26 December 2019. Downloaded on 2/19/2026 12:47:17 PM.
This article is licensed under a Creative Commons Attribution-NonCommercial 3.0 Unported Licence.

Open Access Article. Published on 26 December 2019. Downloaded on 2/19/2026 12:47:17 PM.
This article is licensed under a Creative Commons Attribution-NonCommercial 3.0 Unported Licence.

mA h g^{-1}, both of which are much higher than that of the $LiMO_2$ cathodes (less than 200 mA h g^{-1}).[10] Moreover, MCs usually possess better electrical conductivity, thermal stability and mechanical stability than their corresponding metal oxides.[11] Notwithstanding these virtues, the practical application of MCs is still confronted with some serious problems, such as the limited number of accessible active sites, unsatisfactory electrical conductivity, blocked ion and mass transmission channels, knotty shuttle effect of lithium/sodium polysulfides and pronounced volume variation during the discharge/charge process.

To alleviate these problems, diverse strategies, such as microstructure and component modulating,[12] heteroatom doping,[13] and hybridization with conductive matrixes,[14] have been developed. Among these methods, hybridization with conductive matrixes, such as graphene, carbon frameworks, metal foam and foil, is of extraordinary interest given its obvious promotion effects. Distinctively, compared with the open-ended graphene and metal foam/foil, quasi-closed hollow frameworks are more appealing because of their unique intrinsic features including distinguishable interior voids, low density, high loading capacity and high surface-to-volume ratio, as well as short mass- and charge-transport lengths, thus representing a promising avenue for mitigating the above-mentioned obstacles of MCs.[15,16] In general, these nanostructured MCs are encapsulated within the interior space of well-defined hollow frameworks to form confined hollow MCs (CHMCs), the construction of which endows MCs with many new functionalities for various electrochemical systems. To be specific, the nano-sized building blocks of MCs can both offer extra available electroactive sites for energy storage, and improve the tap density of 3D hollow structures. Meanwhile, the hollow shell can ensure an augmented contact area between the electrolyte and electroactive materials, which is beneficial for the fast diffusion of ions/electrons. Besides, it can also act as a barrier to prevent the encapsulated electroactive nanoparticles (NPs) from aggregating and loss. As for the hollow cavity, it can effectively alleviate the pulverization and dissolution of electrode materials by accommodating the pronounced volume variation associated with repeated charging/discharging processes.[17,18] These unique structural characteristics make CHMCs promising electrode materials for diverse energy storage devices, and laudable electrochemical performances in terms of rate capability, specific capacity and cycling stability are achieved.

To date, diverse CHMCs have been created, in which the interior confined MCs mainly exist in the forms of NPs[19] or nanosheets (NSs),[20] while the morphologies of the external shell can be nano/microspheres,[21] polyhedrons,[22] nanotubes,[23] and even nanoflowers.[24] Such multiformity makes CHMCs a charming research topic. In spite of these successes, the study of CHMCs is still in its infancy, and more advanced confined hollow nanostructures with multifunctional compositions and controlled configurations, and related mechanisms remain to be explored. Considering that previous reviews have reported diverse 2D or simple hollow structures of metal sulfides and oxides, and their energy-related applications,[25–29] this review focuses on CHMCs and the correlation between CHMC structural features and their electrochemical behaviours, aiming at providing some insight into the design and synthesis of advanced CHMCs. The content of this review can be divided into three parts: firstly, we summarized the very recent progress in the smart architecture of CHMCs through compositional and geometrical manipulation. Secondly, we systematically discussed the effect of structural engineering on optimizing various electrochemical performances. Increasing the diversity of CHMCs in a designed manner is expected to bring more possibilities in modulating the properties of functional nanostructures for many applications. Lastly, some future investigations on novel CHMCs are proposed to tackle the current and prospective possible challenges.

Dr Jianchun Bao is currently a full professor in the School of Chemistry and Materials Science, Nanjing Normal University. He received his BS degree from Nanjing Normal University in 1983, his MS degree from Nankai University in 1987 and his PhD degree from Nanjing University in 2002. His research interests include inorganic materials chemistry, surface and colloidal chemistry and electrochemistry, with a focus on the design and synthesis of differently shaped functional inorganic materials and their applications in energy storage and conversion, photocatalysis, and sensors.

Results and discussion

Synthesis and formation mechanism of confined hollow structures

The CHMCs covered in this review mainly include sulfides of tin, iron, cobalt, nickel, molybdenum, and tungsten, and selenides of iron, cobalt, and molybdenum, as well as mixed metal sulfides or selenides. Based on their geometric architectures, subunits and chemical compositions, these CHMCs are classified into six categories: (1) double-shelled confined hollow structures with different shapes, such as nanoboxes and dodecahedral confined hollow structures, (2) core–shell confined structures with a hollow cavity, (3) hierarchical NP- and (4) NS-based confined structures encapsulated within different-shaped single-shelled hollow structures, (5) CHMCs with composite structures and (6) composite components (Fig. 1). Importantly, these CHMCs are basically obtained by combinatorial methods, in which a hard template method is firstly employed to establish reaction skeletons while a wealth of template-free methods, including those based on selective etching, ion exchange, Kirkendall effect and Ostwald ripening are subsequently adopted for the construction of the secondary structure. Besides, high temperature annealing is also often used for carbon framework production. Apart from the hard

 This journal is © The Royal Society of Chemistry 2020

Open Access Article. Published on 26 December 2019. Downloaded on 2/19/2026 12:47:17 PM.
This article is licensed under a Creative Commons Attribution-NonCommercial 3.0 Unported Licence.

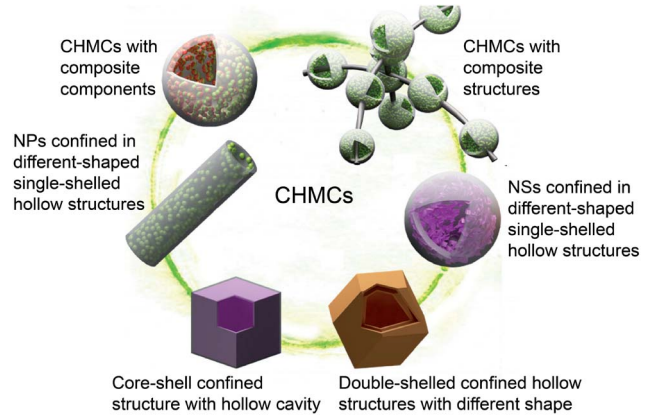

Fig. 1 Classification of different CHMCs.

template method, a solvothermal strategy is usually adopted for the template-free synthesis of CHMCs.

Double-shelled confined hollow structures with different shapes

Double or multi-shelled spherical hollow structures are the most common and available confined architectures adopted in electrochemical fields, but relevant reports are focused on metal oxides and hydroxides.[30,31] Compared with metal oxides, MCs have a multitude of possible stoichiometric compositions, valence states, crystal structures and morphologies, the characteristics of which endow them with higher electrochemical activity.[2] Thus there has recently been an increasing interest in fabricating MC-based confined hollow structures, and studies referenced herein are centred on non-spherical double-shelled CHMCs. Nevertheless, it is much more challenging to construct uniform polyhedral confined hollow structures due to the paucity of applicable anisotropic templates, difficulty in obtaining eligible coatings around high-curvature scaffolds, and poor preservation of shapes with high residual stress.[2,32]

Although with great difficulties, several polyhedral CHMCs still have been successfully created by various ingenious approaches. For instance, hierarchical hollow nanoboxes of NiS with a double-shell have been obtained *via* a facile template-assisted method.[33] As illustrated in Fig. 2a, Fe_2O_3 nanocubes with a uniform size of about 500 nm are firstly prepared as the initial template by a co-precipitation method. Then by means of a modified Stöber method, Fe_2O_3@SiO_2 nanoboxes, in which the SiO_2 coating is measured to be about 100 nm, are obtained. Afterwards, these core–shell nanoboxes are etched with HCl to remove the Fe_2O_3 cores. The obtained SiO_2 hollow nanoboxes not only act as the hard template but also serve as the starting material for subsequent reactions. Concretely, they are hydrothermally treated in Ni^{2+}-containing alkaline solution (100 °C, 12 h) to realize double-shelled nickel silicate ($Ni_3Si_4O_{10}(OH)_2 \cdot 5H_2O$) hollow nanoboxes. Note that the formation of double shells in this process is the result of the nanoscale Kirkendall effect. Because in the hydrothermal process, the silicate anions (originating from SiO_2 dissolution) preferentially react with Ni^{2+}

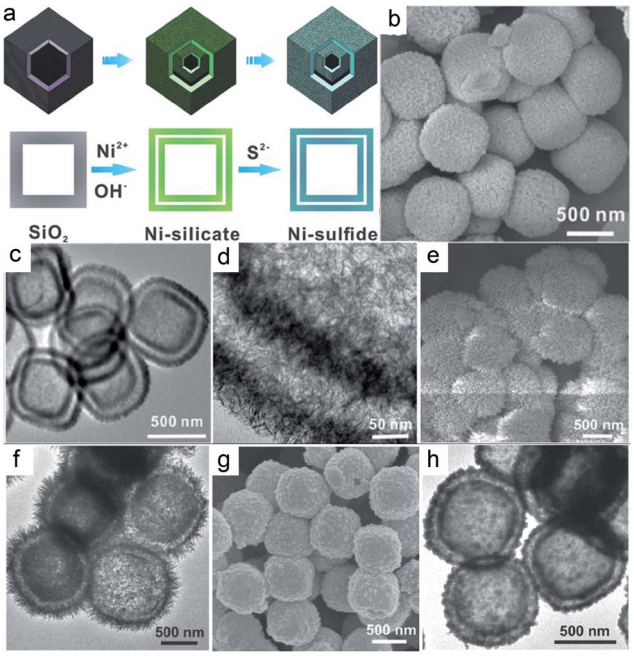

Fig. 2 (a) Schematic illustration of the formation process of the nickel sulfide box-in-box hollow structure. (b) FESEM and (c and d) TEM image of the NiS box-in-box hollow structures. (e) FESEM and (f) TEM images of CuS box-in-box hollow structures. (g) FESEM and (h) TEM images of MnS box-in-box hollow structures. Reproduced from ref. 33, with permission from Wiley, 2014.

to form layered nickel silicate and deposit on the surface of SiO_2 nanoboxes. As the reaction proceeds, SiO_2 continuously dissolves and diffuses outwards, leading to a gap between the remaining SiO_2 core and the nickel silicate shell. When the gap enlarges to a certain degree, the dissolved silicate anions would react with the inwardly diffused Ni^{2+}. As a result, the second nickel silicate shell would form on the surface of the remaining SiO_2 core. After 12 h of continuous reaction, double-shelled hollow nanostructures of nickel silicate are eventually obtained. This process basically does not change the cubic morphology of SiO_2 nanoboxes except for a rougher surface. Finally, the as-prepared nickel silicate nanoboxes are chemically converted into double-shelled NiS hollow nanoboxes through a solution-based sulfidation reaction with Na_2S. Fig. 2b–d display the TEM images of the resultant NiS nanoboxes, from which double-shelled hollow nanostructures with a well-defined pseudo-cubic void are clearly observed. The outer shell shows a similar morphological feature to that of the inner shell, with an obvious gap between them, meaning a unique box-in-box architecture. The thickness of the outer shell is measured to be around 50 nm (Fig. 2c), nearly identical to that of the inner shell. Moreover, both of the double shells are constructed by ultrathin and curved NSs with a small thickness of a few nanometers (Fig. 2d). Then, a high surface area of 140.28 $m^2\ g^{-1}$ and small pore size below 10 nm are achieved for this double-shelled hollow nanobox of NiS. It is noteworthy that this template-assisted synthetic method can also be easily extended to the preparation of other double-shelled hollow metal sulfides, such as CuS

Open Access Article. Published on 26 December 2019. Downloaded on 2/19/2026 12:47:17 PM.
This article is licensed under a Creative Commons Attribution-NonCommercial 3.0 Unported Licence.

(Fig. 2e and f) and MnS (Fig. 2g and h), signifying the universality of such a strategy.

Besides nanoboxes, complicated polyhedrons, such as dodecahedrons and some irregular ones have also been developed with the assistance of different polyhedron templates. For example, Lou's group synthesized a novel double-shelled zinc–cobalt sulfide (Zn-Co-S) rhombic dodecahedral cage (RDC) when a bimetallic zinc/cobalt-based zeolitic imidazolate framework (Zn/Co-ZIF) was employed as the rhombic dodecahedral hard template (Fig. 3a).[34] Briefly, the Zn/Co-ZIF template (with a size of about 1.9 μm) is firstly subjected to selective chemical etching with tannic acid to generate yolk-shelled Zn/Co-ZIF RDCs. Afterwards, these yolk-shelled structures are transformed into the desired double-shelled Zn-Co-S RDCs (with a size of about 1.6 μm) *via* a solvothermal reaction with thioacetamide at 150 °C. The obtained double-shelled hollow nanostructure is similar to the above box-in-box hollow structure of NiS, but obviously, the synthesis of Zn-Co-S RDCs herein is more simple. This is mainly ascribed to their different etching mechanisms. Firstly, tannic acid is easily absorbed on the surface of Zn/Co-ZIF dodecahedrons and protects the dodecahedrons from destruction. Next, tannic acid can hardly penetrate into the body of Zn/Co-ZIF owing to its large molecular size. Consequently, such a surface-functionalized template would enable the selective etching of the unprotected interlayer of Zn/Co-ZIF dodecahedrons, thus contributing to the yolk-shelled Zn/Co-ZIF RDCs. Fig. 3b and c show the SEM images of the resultant Zn-Co-S RDCs, from which well-defined hollow dodecahedrons with double-shells (as revealed by the broken Zn-Co-S RDC shown in Fig. 3c) are clearly observed. The TEM images in Fig. 3d–f indicate that the inner and outer shells of the Zn-Co-S RDCs have a rhombic dodecahedral morphology, both of which are constructed by small NPs. According to energy-dispersive X-ray (EDX) analyses, the Zn/Co molar ratio in Zn-Co-S RDCs is about 0.6 : 1. This value can be simply adjusted by changing the feeding ratio of zinc/cobalt nitrate in the synthesis of Zn/Co-ZIF dodecahedrons, while the related morphology is well maintained.

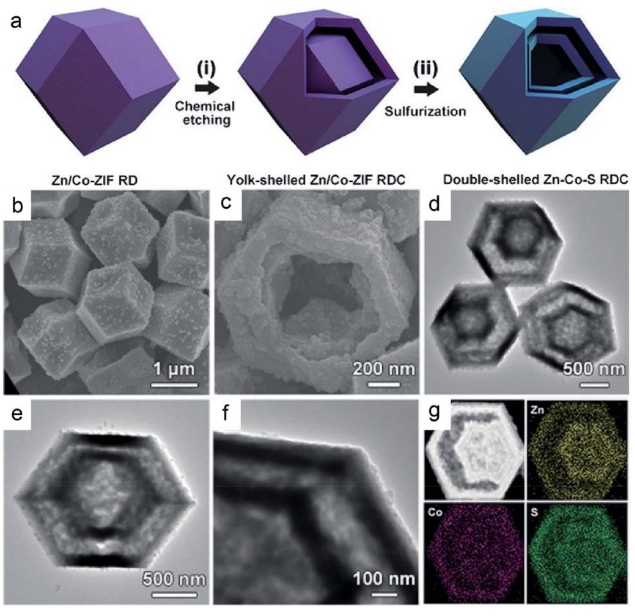

Fig. 3 (a) Schematic illustration of the formation process of double-shelled Zn-Co-S RDCs. (b and c) FESEM, and (d–f) TEM images of the double-shelled Zn-Co-S RDCs. (g) HAADF-STEM image and elemental maps of Zn, Co, and S of a double-shelled Zn-Co-S RDC. Reproduced from ref. 34, with permission from Wiley, 2017.

Core–shell confined structure with a hollow cavity

Besides the above double-shelled hollow structures with space between the shells, there are still some reports on core–shell hollow structures in which the shell is in close contact with the interior cavity.[11,22] A carbonization process is usually involved in their synthesis. Taking the preparation of bullet-like Cu_9S_5@NC hollow NPs as an example, a combinatorial route, including the initial hard template method and subsequent ion exchange and carbonization treatments, is adopted.[22] As illustrated in Fig. 4a, a bullet-like ZnO solid template was firstly prepared by a facile reflux method. Then by means of a facile anion exchange strategy, the above ZnO bullets were sulfurized to form ZnS hollow bullets. To improve the conductivity of the whole nanostructure, a layer of nitrogen-doped carbon shell was subsequently covered on the surface of ZnS to form the ZnS@NC nanostructure *via* coating with polydopamine (PDA) and then annealing at evaluated temperature. Finally, a cation exchange strategy between Zn^{2+} and Cu^{2+} was conducted to realize the construction of desired bullet-like Cu_9S_5@NC hollow nanostructures (Fig. 4b–d). Delightedly, such a self-templating method is also applicable for preparing Cu_9S_5 hollow particles with different shapes, such as hollow spheres, microboxes and nanotubes.

Nanoparticles confined in different-shaped single-shelled hollow structures

Apart from double-shelled confined hollow structures and core–shell confined structures with a hollow cavity, single-shelled hollow structures with diverse electroactive MC NPs embedded in their interior cavities have also been developed. For example,

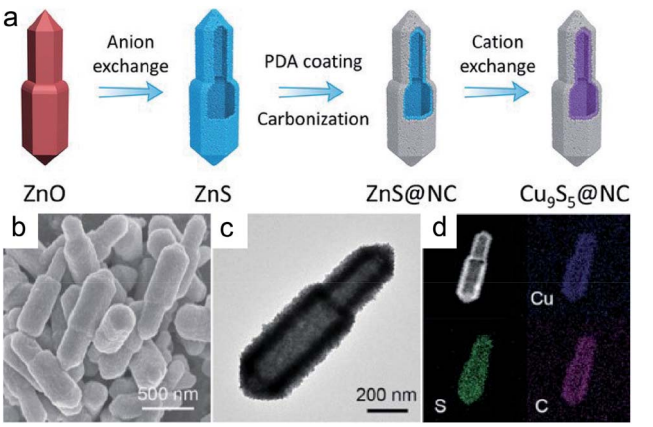

Fig. 4 (a) Schematic illustration of the synthesis of bullet-like Cu_9S_5@NC hollow particles. (b) FESEM, (c) TEM, and (d) elemental mapping images of the Cu_9S_5@NC hollow bullet. Reproduced from ref. 22, with permission from Wiley, 2019.

This journal is © The Royal Society of Chemistry 2020

Open Access Article. Published on 26 December 2019. Downloaded on 2/19/2026 12:47:17 PM.
This article is licensed under a Creative Commons Attribution-NonCommercial 3.0 Unported Licence.

Yoon's group prepared a single-shelled hollow N-doped carbon (NC) sphere encompassing a millerite NiS core (denoted as NiS-NC HS).[35] Fig. 5a schematically illustrates the synthetic procedure of the NiS-NC HS, as well as its Ni_3S_2 and Ni_3S_2-NC counterparts. Briefly, the surface of the metallic Ni templates was firstly coated with a layer of polydopamine (PDA), followed by annealing carbonization to produce Ni-NC NPs. Subsequently, the Ni-NC NPs were partly etched with HCl to create confined Ni-NC HS. Note that a void space (between the NC shell and Ni core) was produced during the etching process, which plays a decisive role in subsequent preparation of the desired NiS-NC HS because appropriate void space can accommodate the volume expansion of the metallic Ni core during the sulfidation process. Otherwise, the NC shells would be broken, leading to a collapsed NC shell accompanied by an aggregated Ni_3S_2 core. Lastly, the above Ni-NC HS was sulfurated with thiourea to realize NiS-NC HS. In the absence of PDA coating and annealing, coalescing metallic-rich Ni_3S_2 NPs are obtained. This means both the envelope of the carbon shell and subsequent etching to release certain free space are necessary for preparing the unique NiS-NC HS.

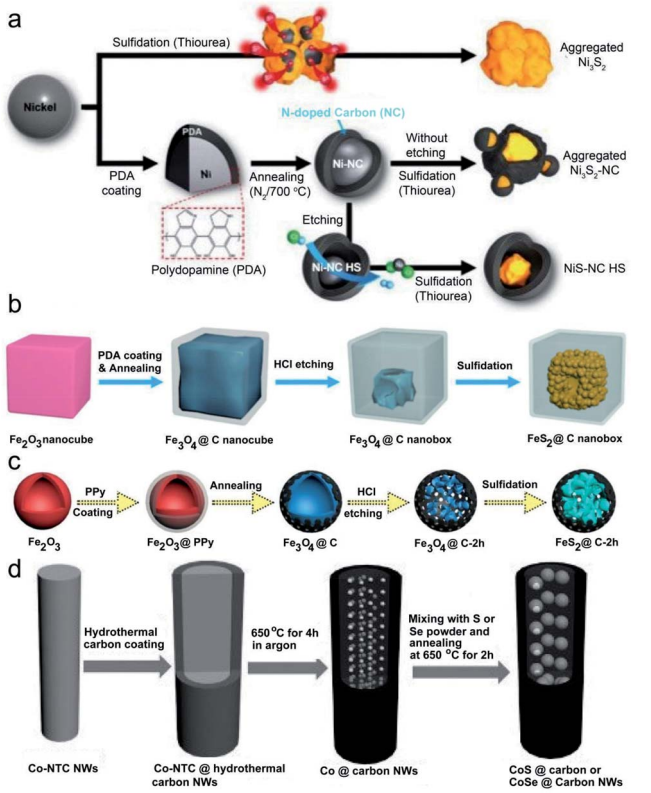

Fig. 5 (a) Schematic illustration of the synthesis of NiS-NC HS in comparison to Ni_3S_2 and Ni_3S_2 NC. Reproduced from ref. 35, with permission from Wiley, 2018. (b) Schematic illustration of the synthesis of FeS_2@C yolk–shell nanoboxes. Reproduced from ref. 36, with permission from the Royal Society of Chemistry, 2017. (c) Schematic illustration of the synthesis of peapod-like CoS⊂carbon NWs and CoSe⊂carbon NWs. Reproduced from ref. 37, with permission from the Royal Society of Chemistry, 2018. (d) Schematic illustration of the synthesis of peapod-like nanoarchitecture. Reproduced from ref. 38, with permission from Wiley, 2016.

Encouragingly, similar synthetic routes, including the initial coating, annealing and subsequent etching, sulfidation or selenization, are also applicable for developing other different component MCs@carbon confined hollow structures. Taking the synthesis of FeS_2@C yolk–shell nanoboxes as an example (Fig. 5b),[36] Fe_2O_3 nanocubes are adopted as the initial template, and then after step-by-step coating, annealing and etching, Fe_3O_4@C nanoboxes are obtained. Such Fe_3O_4@C nanoboxes are finally transformed into the desired FeS_2@C nanoboxes *via* an annealing sulfidation process with sulphur powder based on the reaction of $Fe_3O_4 + 8S \rightarrow 3FeS_2 + 2SO_2\uparrow$, which is different from the above case of NiS-NC HS. The latter is realized by means of a hydrothermal reaction with thiourea ($Ni + H_2S \rightarrow NiS + H_2\uparrow$, H_2S originates from thiourea decomposition). Replacing the Fe_2O_3 nanocubes with Fe_2O_3 hollow spheres, Li *et al.* fabricated a different type of FeS_2@C nanostructure with FeS_2 NSs encapsulated in porous hollow carbon sphere (as displayed in Fig. 5c).[37] The formation of FeS_2 NSs is mainly attributed to the tiny size of the Fe_3O_4 intermediate and thus its ability to be easily vulcanized. Other than the FeS_2@C, peapod-like carbon-encapsulated cobalt chalcogenide nanowires (CoS⊂carbon NWs and CoSe⊂carbon NWs) have also been successfully developed *via* the above method when cobalt-nitrilotriacetic acid (Co-NTC) NWs are selected as the hard template (Fig. 5d).[38] Differently, during the annealing process, the carbon shell is pyrolyzed into amorphous carbon walls and coated on the surface of the initial Co-NTC NWs. Meanwhile, the NTC is pyrolyzed into low density porous carbon cores, and the Co ion is reduced into metal NPs which preferably embed into the porous carbon cores, finally offering peapod-like structured Co⊂carbon NWs. These metallic Co NPs are highly active, and thus would easily allow the permeation of S or Se powder through the carbon layers at high temperature to form the desired CoS⊂carbon and CoSe⊂carbon NWs. Obviously, this "top-down" synthesis approach is similar to the previously reported template-assisted method, but no extra etching step is needed, and thus is of great convenience for broad applications.

Besides nanospheres and nanopolyhedrons, nanotubes (especially carbon nanotubes) have also been frequently adopted as containers for improving the electrochemical performance of various materials. Furthermore, the 1D cavity of carbon nanotubes has been proposed as the nanoreactor for promoting different catalytic reactions (by introducing active materials into the cavity). However, there are few reports related to confined structures of CMs in carbon nanotubes. Apart from the above "top-down" synthetic method, several simple methods using carbon nanotubes as the nanoscale reactor have been developed to prepare CHMCs.[40,41] Zhang and Liu's group adopted a solvothermal and subsequent heat treatment.[39] Fig. 6a depicts the detailed synthetic procedure of the Fe–S@CNT, which mainly includes (1) vapor deposition of sulfur/ferrocene into the hollow nanochannels of CNTs to form S-ferrocene@CNTs; (2) annealing in an inert atmosphere for producing Fe–S NPs inside the CNTs (Fe–S@CNTs). The CNTs herein are of great importance in stimulating the decomposition of ferrocene and subsequent sulfidation because the interior of CNTs has a strong affinity for the reactant molecules,

Open Access Article. Published on 26 December 2019. Downloaded on 2/19/2026 12:47:17 PM.
This article is licensed under a Creative Commons Attribution-NonCommercial 3.0 Unported Licence.

creating a higher local concentration and pressure of reactants inside the CNT reactor than the open environment, and thus finally increases the reaction rate and yield. Besides, by means of a facile *in situ* chemical transformation, Sun's group designed a novel bamboo-like confined hollow structure with $Fe_{1-x}S$ NPs encapsulated within bamboo-like carbon nanotubes (Fe_{1-x}-S@CNTs).[40] Importantly, these composites are cross-linked with each other to form a 3D network, which can serve as a conductive highway for rapid electron transportation. Fig. 6b shows the template-free formation process of the delicate $Fe_{1-x}S$@CNTs. To be specific, a mixture of melamine and $FeCl_3$, obtained from sustaining stirring at low temperature and mechanical grinding, was firstly pyrolyzed under an inert atmosphere to produce an Fe-based precursor. During this process, melamine was decomposed and the released C/N species liberally cracked on the surface of Fe particles (derived from $FeCl_3$ decomposition), followed by diffusion into the particles to form the Fe_3C/Fe@CNT composite. Moreover, numerous pores were generated under this process, contributing to a high surface area of 269.5 $m^2\ g^{-1}$ and pore volume of 0.674 $cm^{-3}\ g^{-1}$. Finally, the Fe_3C/Fe@CNTs were *in situ* chemically converted to the Fe_{1-x}-S@CNTs composite by means of annealing with sulfur powder. Fig. 6c–f present the morphology and microstructure characteristics of the above $Fe_{1-x}S$@CNTs, and a hollow bamboo-like morphology with a diameter of 20–50 nm was observed. Moreover, the encapsulated $Fe_{1-x}S$ NPs are highly dispersed throughout the CNTs (not limited to the end). Such a template-free synthetic approach will simplify the experimental procedures and omit the consequent treatment of removing the template.

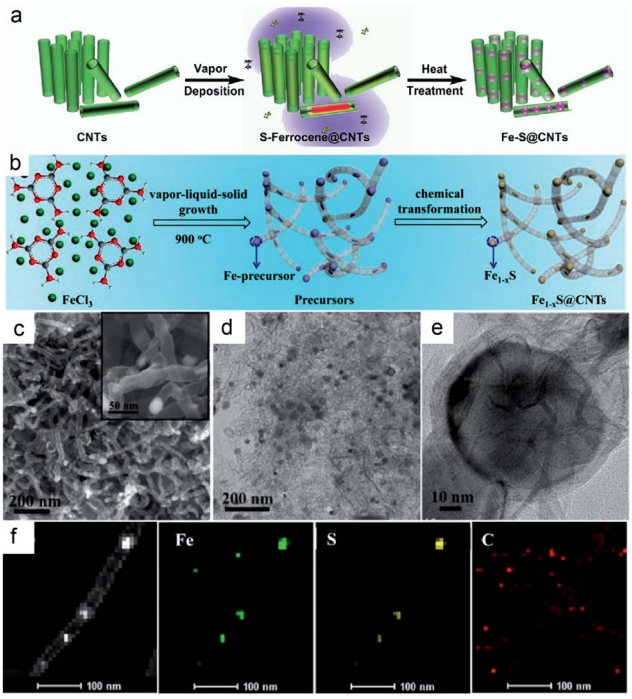

Fig. 6 (a) Schematic illustration of the synthesis of Fe–S@CNT. Reproduced from ref. 39, with permission from Wiley, 2016. (b) Schematic illustration of the synthesis of $Fe_{1-x}S$@CNTs. (c) SEM (d) TEM (e) HRTEM (f) STEM and corresponding elemental mapping images of the $Fe_{1-x}S$@CNTs. Reproduced from ref. 40, with permission from American Chemical Society, 2017.

Nanosheets confined in different-shaped single-shelled hollow structures

Recently, the synthesis of confined MCs NSs in different-shaped single-shelled hollow structures has become a hot research topic due to the unique structural virtues of 2D NSs, such as high specific surface area, short ion transport paths and rich physicochemical properties. For instance, Chen's group fabricated a novel confined hollow structure with petal-like MoS_2 NSs embedded in hollow mesoporous carbon spheres (HMCSs) (denoted as MoS_2@C).[41] Fig. 7 displays the multi-step synthetic route, in which tetraethylorthosilicate (TEOS) and resorcinol formaldehyde (RF) oligomers are firstly co-condensed on SiO_2 particles to form the SiO_2@SiO_2/RF core–shell nanostructure (average size of 320 ± 30 nm). Secondly, these SiO_2@SiO_2/RFs are transformed into SiO_2@SiO_2/C nanospheres *via* calcination and carbonization. Thirdly, the SiO_2 cores are chemically etched by NaOH to generate HMCSs. Lastly and most importantly, a hydrothermal method is employed to grow MoS_2 NSs in the cavities of the HMCSs, in which process HMCSs play crucial roles in achieving the desired petal-like MoS_2@C yolk–shell structure. Concretely, under hydrothermal conditions, thiourea can easily react with water to produce H_2S gas, which tends to adsorb on the rough inner wall of HMCSs. Meanwhile, the MoO_4^{2-} diffuses into the hollow cavity of HMCSs freely *via* the mesoporous shell. Upon the accumulation of H_2S to a certain concentration, it would react with the interior MoO_4^{2-}, leading to the formation of the MoS_2 crystal nucleus inside the HMCSs. Afterwards, the HMCSs would act as nanoreactors to support the continuous confined growth of MoS_2 NSs, and finally give rise to the petal-like MoS_2@C. Note that if the mesoporous carbon shell is replaced by an ordinary one without mesoporous, the MoS_2 NSs will directly grow on the outside surface of the carbon shell, which structure is easily broken during long-term cycling tests if applied in battery devices.

Delightedly, the above synthetic approach is also applicable for preparing other metal sulfides@carbon yolk–shell structures.

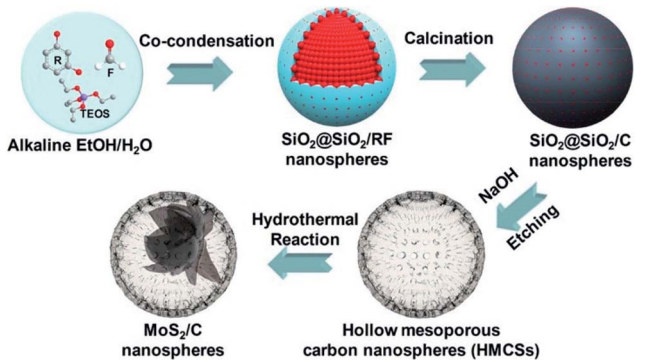

Fig. 7 Schematic illustration of the synthesis of yolk–shell MoS_2@C nanospheres. Reproduced from ref. 41, with permission from American Chemical Society, 2017.

This journal is © The Royal Society of Chemistry 2020

Open Access Article. Published on 26 December 2019. Downloaded on 2/19/2026 12:47:17 PM.
This article is licensed under a Creative Commons Attribution-NonCommercial 3.0 Unported Licence.

As an example, replacing $Na_2MoO_4 \cdot 2H_2O$ and thiourea with $WCl_6 \cdot 2H_2O$ and thioacetamide, hierarchical triple-shelled WS_2–C–WS_2 hollow nanospheres (denoted as HTSHNs WS_2/C) with ultrathin WS_2 NSs perpendicularly connected within the HMCS scaffold are obtained (Fig. 8).[42] What's different is that the metal cations (W^{6+}) herein are electrostatically adsorbed onto the HMCSs, followed by hydrolysis to form WO_x nanocrystals dispersed inside and outside the carbon walls. Finally, these WO_x nanocrystals are converted to WS_2 NSs through the hydrothermal reaction with H_2S. Besides metal sulfides, the above synthetic approach can also be applied to the construction of metal selenides. For example, Sun's group fabricated an encapsulated-type confined hollow structure comprising hollow carbon nanospheres (HCNSs) and few-layer $MoSe_2$ NSs with expanded (002) planes.[43] A mixture of selenium powder (Se) and hydrazine hydrate ($N_2H_4H_2O$, 80%) is selected as the selenide precursor herein. The production of expanded (002) planes for $MoSe_2$ is due to the intercalating effect (*i.e.*, restricting the growth of $MoSe_2$ NSs over certain planes) of ethylenediamine (H_2N–CH_2–CH_2–NH_2). Moreover, it also controls the 2D growth of $MoSe_2$ in the hollow carbon shell frameworks to generate few-layer structures. As a result, the unique carbon-stabilized $MoSe_2$@HCNS hybrid framework with expanded (002) crystal planes and few-layer $MoSe_2$ NSs is realized.

The above CHMCs with NSs inside are synthesized using the SiO_2 template. Our group and the Lou group have recently developed a series of advanced structures with SnS_2 NSs confined within different-shaped hollow carbon shells by simply changing the template adopted.[20] As displayed in Fig. 9, uniform MnO_x nanorods, Fe_2O_3 nanocubes, and SiO_2 nanospheres are employed as the initial templates. Then by means of a simple solvothermal reaction, a layer of SnO_2 nanocrystals is grown on their surface to form the core–shell structured MnO_x@SnO_2 nanorods, Fe_2O_3@SnO_2 nanocubes, and SiO_2@SnO_2 nanospheres, Subsequently, dopamine polymerization (to form polydopamine PDA) is carried out on the surface of the above core–shell nanostructures, followed by selective etching with oxalic acid to produce SnO_2@PDA hollow structures. Note that NaOH can etch PDA, and thus the SiO_2 cores in the SiO_2@SnO_2 nanospheres are firstly removed with NaOH, and next, PDA coating is conducted. Afterwards, the above SnO_2@PDA hollow structures are annealed at 500 °C under an Ar atmosphere to generate well-crystallized SnO_2@C nanotubes, nanoboxes, and hollow nanospheres, respectively. Finally, these SnO_2@C nanostructures are sulfurized at 350 °C under an H_2S/Ar atmosphere to achieve the desired SnS_2@CNTs, SnS_2@CNBs, and SnS_2@CNSs, respectively. Such a general templating strategy can also be extended to many other similar MCs for catalysis or energy related applications.

Distinctively, by means of a well-designed template-free solvothermal method and carbonization treatment, Jiao and Feng's group created a porous hierarchical structure of Co_9S_8@carbon hollow microspheres (Co_9S_8@CHSs).[44] Fig. 10 shows the detailed template-free preparation procedure of the Co_9S_8@CHSs, which mainly includes the production of Co_9S_8@C precursor microspheres with hierarchical hollow structures, and subsequent transformation to the desired Co_9S_8@CHSs. Specifically, in the solvothermal system with glucose, thiourea and Co^{2+} dispersed in mixed solvent (EG and DMF), plenty of microspheres covered with flimsy carbon layers were firstly formed within a very short time and some of them evolved into core–shell structures when the reaction proceeds to about 1 h. Increasing the reaction time to 2 h, a folded carbon layer emerged which covered the surface of the spheres, and the spheres changed from core–shell to hollow structure. With the prolongation of reaction time, the thickness of the carbon layer increases gradually and the hollow structure has been formed completely after 6 h. Obviously, the generation of the hollow structure of Co_9S_8@CHSs should be ascribed to the Kirkendall effect. Such a template-free hydrothermal strategy is simple, environment-friendly and easy to operate, and thus is

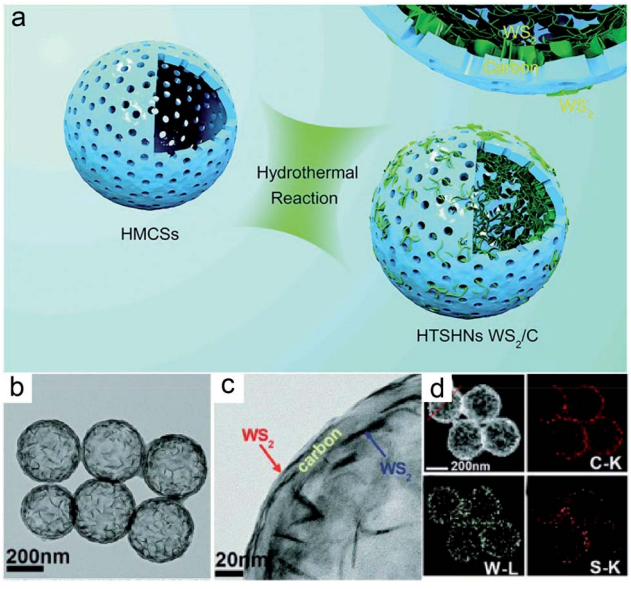

Fig. 8 (a) Concept of synthesizing HTSHNs WS_2/C. (b and c) TEM, (d) STEM and the corresponding EDX elemental maps of C, W, and S of HTSHNs WS_2/C composites. Reproduced from ref. 42, with permission from the Royal Society of Chemistry, 2018.

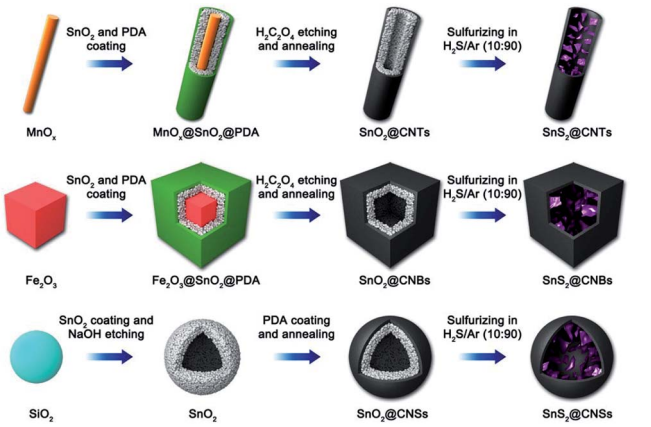

Fig. 9 Schematic illustration of the synthesis processes of SnS_2@CNTs, SnS_2@CNBs, and SnS_2@CNSs. Reproduced from ref. 20, with permission from Elsevier, 2018.

Open Access Article. Published on 26 December 2019. Downloaded on 2/19/2026 12:47:17 PM.
This article is licensed under a Creative Commons Attribution-NonCommercial 3.0 Unported Licence.

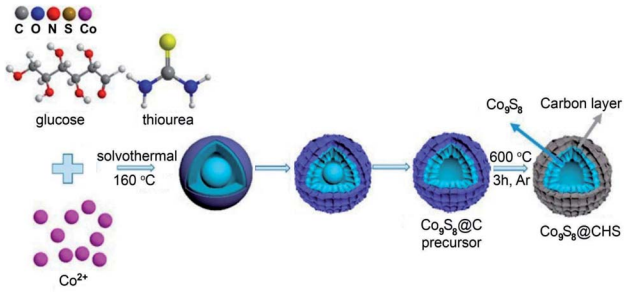

Fig. 10 Schematic diagram of the synthesis route for Co_9S_8@CHSs. Reproduced from ref. 44, with permission from American Chemical Society, 2019.

advantageous for advancing a wealth of other confined hollow structures of MCs. For instance, Qian and Zhu's group employed such a strategy for preparing MoS_2@C hollow nanotubes.[23] Briefly, the $Mo_3O_{10}(C_2H_{10}N_2)$ nanowire was firstly fabricated consulting the reported method, and then it was hydrothermally sulfurated to realize the desired MoS_2@C hollow nanotube in the presence of glucose. When the reaction time proceeds to 2 h, some NSs emerged on the surface of the initial nanowires and amorphous carbon formed synchronically. As the time expands to 8 h, the central part of the initial nanowire becomes transparent, suggesting the transformation of $Mo_3O_{10}(C_2H_{10}N_2)$ to MoS_2. Such conversion is basically completed until the reaction time achieves 12 h, accompanied by the generation of the carbon shell originating from glucose carbonization. These results indicate that the formation of the hollow structure should also be ascribed to the Kirkendall effect, in which process MoS_2 is formed based on the continuous consumption of MoO_3. Notably, it was found that, in the absence of glucose, MoS_2 microflowers (rather than nanotubes) comprised of aggregated MoS_2 NSs, are obtained. The main reason is that carbon takes shape along with the formation of MoS_2 NSs, and the formed carbon shell can maintain the tubular-like morphology of MoS_2 during the subsequent sulfuration process. This explanation is consistent with the formation of the above Co_9S_8@CHSs, *i.e.*, without the tubular carbon shell to fix the shape, spherical nanostructures are obtained.

CHMCS with composite structures

Increasing the structural diversity of CHMCs can improve or even change the electrochemical behaviors of the resultant composite materials owing to the advantages and synergetic effects of different microstructures themselves.[45] Generally, the structural diversification units can be 1D nanowires/nanotubes, 2D NSs or 3D nanoframes/skeletons. For example, Jin and coworkers developed a sulfur host material in which Co_3S_4 nanoboxes are connected in series by 1D CNTs, forming an integrated conductive network (S@CNTs/Co_3S_4-NBs).[46] Such implant structure will boost the electrical conductivity of the sulfur species encapsulated in Co_3S_4-NBs, thus greatly enhancing the utilization rate of sulfur species. Fig. 11a presents the self-template synthetic process of the S@CNTs/Co_3S_4-NBs with three steps. Firstly, uniform ZIF-67 nanocubes were *in situ* nucleated, grown and threaded on carboxyl group (–COOH) functionalized CNTs to produce the CNTs/ZIF-67 precursor. Afterwards, this precursor was chemically converted to CNTs/Co_3S_4-NBs by means of solvothermal sulfuration and subsequent annealing treatments. Herein, a Kirkendall effect is responsible for the formation of hollow Co_3S_4-NBs due to the different diffusion rates of cobalt and sulfur species. Finally, a melt-diffusion method is employed to enrich the interior cavity of the above Co_3S_4-NBs with sulfur, leading to the desired S@CNTs/Co_3S_4-NB composite. In addition to this 1D CNT connected composite structure, Wang *et al.* fabricated a graphene sandwiched composite with SnS@C nanospheres intercalated in 2D graphene lamella (SnS@C-rGO), forming a honeycomb-like network architecture.[47] The SnS@C nanospheres herein are constructed from nanoscale SnS NSs and hollow mesoporous carbon spheres, which could enable fast ion transport kinetics arising from decreased diffusion pathways. Moreover, their interconnected framework could enhance the electrical conductivity of the whole electrode. Fig. 11b reveals the formation process of the SnS@C-rGO composite, which is similar to that of the above petal-like MoS_2@C structure, but the resultant yolk–shell nanospheres are further confined within GO NSs, followed by calcination to realize the desired SnS@C-rGO nanocomposite.

Besides, Sun and Wu's group developed a more complicated composite consisting of cobalt sulfide quantum dots (Co_9S_8 QDs with size less than 4 nm), mesoporous hollow carbon polyhedral (HCP) and 3D reduced graphene oxide (rGO) nanoframes to form a hierarchical sponge-like architecture.[48] Specifically, the Co_9S_8 QDs are homogeneously embedded in the HCP matrix, which is further encapsulated in the macropores of the 3D rGO framework, forming a double carbon-confined hierarchical composite. Such a composite has colorful structural characteristics: (1) the HCP can prevent the excessive growth and aggregation of Co_9S_8 QDs, as well as expanding their lattice parameters for enhanced reactivity; (2)

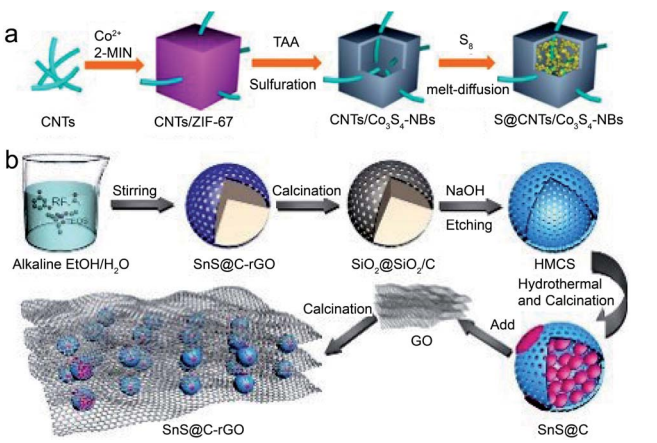

Fig. 11 Schematic illustration of the synthesis of (a) S@CNTs/Co_3S_4-NBs. Reproduced from ref. 46, with permission from American Chemical Society, 2017. (b) Schematic illustration of the synthesis of the 3D SnS@C-rGO nanocomposite. Reproduced from ref. 47, with permission from Wiley, 2019.

This journal is © The Royal Society of Chemistry 2020

Open Access Article. Published on 26 December 2019. Downloaded on 2/19/2026 12:47:17 PM.
This article is licensed under a Creative Commons Attribution-NonCommercial 3.0 Unported Licence.

the rGO skeleton and HCP can provide double confinement for fixing and dispersing the host Co_9S_8 QDs; (3) such an integrated composite enables rapid electron transfer and prevents the additional capacity originated from the conductive agents. Obviously, this (Co_9S_8 QD@HCP) @rGO composite has extraordinary traits for energy storage systems compared with conventional Co_9S_8@C or Co_9S_8-C materials. Fig. 12 illustrates the ice-template-assisted combinatorial synthesis procedure of the (Co_9S_8 QD@HCP) @rGO composite, which mainly includes three steps: firstly, positively charged Co^{2+} was adsorbed onto the surface of negatively charged GO through electrostatic interactions. Then 2-methylimidazole was added and *in situ* grown to form a Co-based zeolitic imidazolate framework (ZIF-67) crystal on the surface of GO (ZIF-67@GO). Secondly, such a ZIF-67@GO suspension was frozen at −15 °C to obtain an ice crystal, followed by freeze drying to generate the ZIF-67@GO sponge-like precursor. The formation of the 3D scaffold sponge structure is the result of the removal of residual water molecules by high vacuum sublimation while the ice crystal acts as the template. Thirdly, after a simultaneous thermal reduction, carbonization and sulfidation of the above precursor, desired sponge-like (Co_9S_8 QD@HCP) @rGO composites are created. During this annealing process, the central cobalt ions and organic ligands from ZIF-67 were converted into Co_9S_8 QDs and HCP, respectively, while the GO was reduced to macroporous 3D rGO.

CHMCS with composite components

In order to meet some special needs for catalysis or energy systems, the rational design and construction of multi-component confined hollow structures comprising two or more reactive components with individual characteristics are desired.[45] For example, ZnSe is a promising anode material for LIBs/SIBs owing to its high theoretical capacities and the abundance of zinc. However, the low electronic conductivity and enormous volume variation (during the charge–discharge process) of ZnSe make its application a great challenge. As a typical layered metal chalcogenide, $MoSe_2$ has exhibited favorable performance for energy storage devices thanks to its large interlayer spacing (0.65 nm) and higher electrical conductivity. Therefore, the combination of ZnSe and MoSe is of great possibility for overcoming the drawbacks of the individual component and achieving commendable electrochemical performances. Chen and Qian's group has recently prepared a multi-component confined hollow structure with few-layered $MoSe_2$ NSs and ultra-small ZnSe NPs homogeneously confined in a porous carbon matrix.[18] The $MoSe_2$ NSs herein are grown uniformly around the ZnSe NPs. Fig. 13a displays the template-free synthetic procedure of the above advanced ZnSe/$MoSe_2$@C structure. To be specific, Keggin-type heteropolyanions (POMs) and $H_3PMo_{12}O_{40}$ (PMA) (used as the Mo precursor) were firstly embedded into the customized cavities of ZIF-8 (serving as the Zn precursor) to form polymetallic MOFs *via* a self-assembly process. Then, by means of a facile annealing selenization strategy, few-layer $MoSe_2$ NSs were grown around the ZnSe NPs, both of which were confined within the hollow porous carbon spheres, forming the desired ZnSe/$MoSe_2$@C structure. In this step, Zn^{2+} clusters react with Se powder to form ZnSe NPs while the Mo species is reduced synchronously to form laminar $MoSe_2$. The generation of the interior hollow architecture is ascribed to the utilization of PMA as the guest and the removal of excess organic solvent molecules during the selenization process. Other than the above hybrid nanostructure composed of two sole MCs, confined bimetallic or multi-MCs can also function well in various electrochemical fields due to the synergistic effect between different metal atoms. As an example, Li *et al.* synthesized a hollow bimetallic sulfide nanosphere assembled from $NiCo_2S_4$ NPs embedded in ultrathin carbon NSs ($NiCo_2S_4$@C HNSs).[49] Fig. 13b illustrates the detailed preparation process, which mainly includes the initial template-assisted precipitation of the NiCo precursor and subsequent *in situ* chemical conversion to $NiCo_2S_4$. Concretely, monodisperse SiO_2 nanospheres were firstly activated in alkaline urea solution. Then under high-temperature hydrothermal conditions,

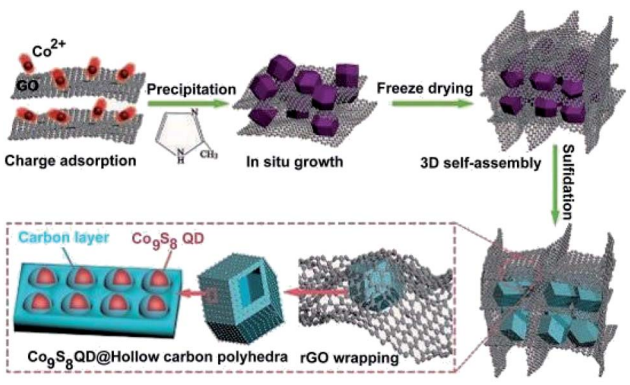

Fig. 12 Schematic illustration of the fabrication procedure of (Co_9S_8 QD@HCP) @rGO sponge-like composites. Reproduced from ref. 48, with permission from Wiley, 2017.

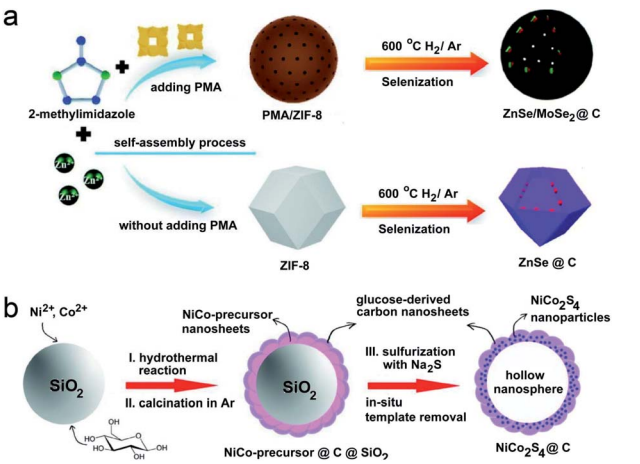

Fig. 13 (a) Schematic synthesis of ZnSe/$MoSe_2$@C and ZnSe@C nanocomposites. Reproduced from ref. 18, with permission from the Royal Society of Chemistry, 2019. (b) Schematic synthesis of $NiCo_2S_4$@C HNSs. Reproduced from ref. 49, with permission from the Royal Society of Chemistry, 2017.

Open Access Article. Published on 26 December 2019. Downloaded on 2/19/2026 12:47:17 PM.
This article is licensed under a Creative Commons Attribution-NonCommercial 3.0 Unported Licence.

the interfacial reaction between activated SiO_2 and different metal ions occurs, leading to the formation and deposition of $Ni_{2/3}Co_{4/3}(CO_3)(OH)_2$ NSs around SiO_2. Meanwhile, glucose is incorporated into carbon NSs, forming an interconnected NS-assembled shell which is uniformly coated on the SiO_2 surface. Afterwards, this carbon shell is graphitized *via* calcination in Ar to create the NiCo-precursor@C@SiO_2 nanostructure. Lastly and importantly, by means of a sulfurization reaction with Na_2S, the above NiCo-precursor@C@SiO_2 material is chemically converted into $NiCo_2S_4$@C hollow nanospheres. The production of the hollow cavity is ascribed to the etching of the SiO_2 core by OH^- released from S^{2-} hydrolysis. Moreover, along with the phase conversion from the NiCo-precursor into $NiCo_2S_4$, its structure transforms from NSs into scattered NPs due to the anion exchange reaction (Kirkendall effect) during the sulfurization reaction with continuous outward ion diffusion. Remarkably, benefiting from the *in situ* template removal strategy, the obtained $NiCo_2S_4$@C HNSs show uniform size, abundant mesopores and robust structure. Besides, the design of carbon NSs may also favor the structural stability, for that the connected carbon NS assembly can relieve the collapse of the hollow structures during the template removal process. These merits endow the $NiCo_2S_4$@C HNSs with remarkable advantages for application in electrochemical systems.

Apart from the above hybrid nanostructures and binary metal sulfides/selenides, doping of a small quantity of metal ions is also appealing for improving the electron transport, rate capability and cycle life of the resultant electrode materials. Typically, Lou *et al.* synthesized hierarchical Cu-doped $CoSe_2$ microboxes constructed by ultrathin NSs *via* a facile two-step sequential ion exchange method.[13] Fig. 14a schematically illustrates the formation process of the Cu-doped $CoSe_2$ microboxes, and Co–Co Prussian blue analogue (PBA) microcubes, prepared by a precipitation method, are selected as the starting material. Then, by means of an anion-exchange reaction with Se^{2-} ions, Co–Co PBA was transformed into hierarchical $CoSe_2$ microboxes assembled from ultrathin NSs. Finally, a cation-exchange approach was conducted to achieve the doping of Cu^{2+} into $CoSe_2$ microboxes. Besides, Wang and Qin's group fabricated a porous bamboo-like hollow tube composed of N-doped-C and MoS_2 layers aligned vertically in an alternating sequence (MoS_2/N-doped-C).[50] Fig. 14b illustrates the synthetic process, which mainly includes (1) the fabrication of MoS_2/oleylamine (OAm) tubes by a solvothermal method and (2) further annealing transformation to MoS_2/N-doped-C. In the solvothermal process, MoO_3 (Mo precursor) firstly reacted with S^{2-} (released from S powder) to generate MoS_2, and OAm intercalated into the interspaces of MoS_2 layers synchronously. Such an organic/inorganic hybrid tube is formed based on a new formation mechanism, and ethanol/water mixed solvent and OAm additive play key roles in this process. In the presence of pure ethanol or water, only irregular particles were obtained, while in the absence of OAm, no tube structure was observed. Water may change the polarity of ethanol, then affects the process of OAm-capping primary MoS_2 monolayers and finally leads to the self-assembly of tubes. OAm serves as both the capping agent to intercalate between MoS_2 layers/encapsulate monolayer MoS_2, and the N-doped-carbon source for subsequent conversion of MoS_2/OAm to MoS_2/N doped-C tubes through annealing.

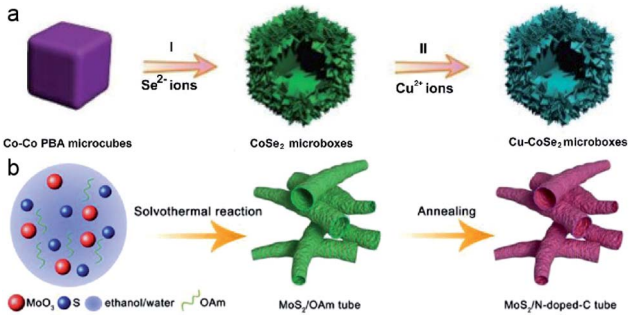

Fig. 14 (a) Schematic synthesis of Cu–$CoSe_2$ microboxes with two-step ion-exchange reactions. Reproduced from ref. 13, with permission from Wiley, 2018. (b) Schematic synthesis of MoS_2/N-doped-C tube. Reproduced from ref. 50, with permission from Wiley, 2018.

Table 1 summarizes the synthetic route, template and formation principle of diverse CHMCs reported in recent years, some of which representative works have been introduced and analyzed in detail above. By classification and comparison, it is found that the synthetic routes mainly include the hydrothermal process, ion exchange, sulfidation/selenization, surface coating, annealing carbonization, chemical etching, *etc.*, in which the etching is usually realized with HF, NaOH, HCl, oxalic acid or OH^- released from the hydrolysis of sulfide ions. Oxides (such as Cu_2O, Fe_2O_3, and SiO_2), MOF, metallic Ni, carbon sphere/tube, and some metal complexes are mostly adopted as templates to prepare confined hollow structures with different morphologies. Moreover, besides the etching methods, the interior void is basically achieved based on the principles of (1) Kirkendall effect, (2) Ostwald ripening, (3) galvanic replacement, (4) chemical etching, (5) solid-state decomposition and (6) dissolution–recrystallization. The construction of precursors, development of new templates, and control of reaction kinetics are of great importance for developing new synthetic strategies and novel CHMCs.

Applications in electrochemical energy storage and conversion

Lithium-ion batteries. Lithium ion batteries (LIBs) have been the most prevailing and mainstream energy storage devices for portable electronics, electric vehicles and grid-scale energy storage systems so far.[76,77] Graphite and $LiCoO_2$ are the currently commercially used anode and cathode materials for LIBs, respectively, based on the reaction $LiCoO_2 + C_6 \rightarrow Li_{1-x}CoO_2 + Li_xC_6$. However, with the increasing demand for energy density and cycle life, the theoretical specific capacity of the graphite anode (372 mA h g^{-1}) can't meet people's requirements anymore.[53,78] One basic reason is that graphite is a single-electron-controlled anode, limiting the improvement of energy density.[79] According to the target set by the US Department of Energy's EV Everywhere Grand Challenge, 250–300 miles per charge for the next generation of electric-driven cars should be

 This journal is © The Royal Society of Chemistry 2020

Open Access Article. Published on 26 December 2019. Downloaded on 2/19/2026 12:47:17 PM.
This article is licensed under a Creative Commons Attribution-NonCommercial 3.0 Unported Licence.

Table 1 Summary of the synthesis details of different CHMCs

Types of materials	Component	Template	Synthesis route	Interior void formation principle	Reference
Double-shelled nanobox	CuS@CoS_2 NS	Cu_2O, $Co(OH)_2$	Sulfidation and etching	Etching with $Na_2S_2O_3$ solution	7
Double-shelled dodecahedral cage	Zn-Co-S	Zn/Co-ZIF rhombic dodecahedron	Sequential chemical etching and hydrothermal sulfurization	Etching with tannic acid	34
Double-shelled hollow structure	CoS NPs/CoS NS	ZIF-67 nanocube	Sequential modulation of template-assisted reactions of ZIF-67 with water and Na_2S	Kirkendall effect	6
Box-in-box hollow structure	MS (M: Ni, Cu, Mn) NSs	Fe_2O_3 nanobox	Hydrolysis and sulfidation	SiO_2 dissolving partially	33
Bullet-like hollow nanostructure	Cu_9S_5@NC	Bullet-like ZnO particle	Ion exchange and PDA coating and carbonization	Diffusion effect	22
Double-shelled hollow sphere	Nitrogen-doped double-shelled hollow carbon spheres-sulfur hybrid	TiO_2 hollow sphere	Carbonization, etching and melt infiltration	Etching with HF	17
Hollow NPs embedded in a nanocage	$Co_9S_8 \subset C$	ZIF-67 rhombic dodecahedral nanocrystal	Annealing and sulfidation	Kirkendall effect	51
"Brain-coral-like" mesoporous hollow confined structure	CoS_2@N-doped C	ZIF-67 hollow sphere	Room-temperature solution method, carbonization, sulfidation and etching	Removal of cobalt by HCl etching	52
Yolk–shell nanobox	FeS_2@C	Fe_2O_3 nanocube	Annealing, etching and sulfidation	Etching with HCl	36
NP inlaid hollow nanopolyhedron	Co_9S_8/C–S	ZIF-67 nanopolyhedron	Sulfidation annealing, and sulfur impregnation	Kirkendall effect	4
Nanodots confined within a porous network	ZnSe@N-doped carbon	Rhombic dodecahedral ZIF-8	Pyrolysis and selenization	Pyrolysis and carbonization	53
NSs in a hollow nanostructure	SnS_2@CNT; SnS_2@CNB; SnS_2@CNS	MnO_x nanorod; Fe_2O_3 nanocube; SiO_2 nanosphere	Hydrothermal treatment, annealing and sulfurization	$H_2C_2O_4$ etching; NaOH etching	20
NSs confined in a hollow nanosphere	$MoSe_2$@C	SiO_2@SiO_2/C	Hydrothermal treatment and confined growth of $MoSe_2$ in a nanoreactor and etching	Etching with NaOH	43
NSs@hollow mesoporous sphere	SnS@C-rGO	SiO_2@SiO_2/RF	Hydrothermal treatment, calcination and etching	Etching with NaOH	47
NSs@3D porous sphere	FeS_2@C	Hollow Fe_2O_3 nanosphere	Annealing, etching and sulfidation	—	37
Petal-like NSs in hollow mesoporous spheres	MoS_2/C	SiO_2@SiO_2/RF nanosphere	Calcination, hydrothermal treatment and etching	Etching with NaOH	41
Hybrid nanobox	CoSe@C	ZIF-67 nanocube	Annealing and selenization	Diffusion effect	54
Core–hollow shell structure	NiS–C	Metallic Ni	Annealing, sulfidation and etching	Etching with HCl	35
Coconut-like core/shell hollow nanosphere	SnS/C	SnO_2 hollow nanosphere	Micro-evaporation-plating and annealing/sulfidation and etching	Etching with NaOH	55
Sheet-on-sheet structured hollow nanosphere	MoS_2/C	—	Polymerization of dopamine hydrochloride with $Mo_7O_{24}^{6-}$ assisted by metal chelation and sulfuration	Tuning volume ratio of ethanol–water	56
A triple shell structure: NSs vertically embedded in a hollow mesoporous sphere	WS_2–C	Hollow mesoporous carbon sphere	Hydrothermal treatment	—	42

Open Access Article. Published on 26 December 2019. Downloaded on 2/19/2026 12:47:17 PM.
This article is licensed under a Creative Commons Attribution-NonCommercial 3.0 Unported Licence.

Table 1 (*Contd.*)

Types of materials	Component	Template	Synthesis route	Interior void formation principle	Reference
Hierarchical nanostructures@hollow microsphere	Co_9S_8@C	—	Hydrothermal treatment and carbonization	Kirkendall effect	44
NPs distributed on a 3D hollow sphere	NiS@C	SiO_2 nanosphere	Annealing, sulfidation and etching	Etching with OH^- released from the hydrolysis of sulfide ions	21
3D porous interconnected nanostructure	SnS/C	Sn^{2+}–L-cysteine complex	Electrostatic spray deposition and annealing	—	57
Hollow heterostructure	Co_3S_4@MoS_2	ZIF-67 polyhedron	Two-step temperature-assisted hydrothermal synthesis and annealing	Diffusion effect	58
Hierarchical nanotubes constructed by NSs	SnS@C	MoO_3 nanorod	Solvothermal treament, annealing and etching	Etching with ammonia	59
NPs confined within a hollow porous sphere	ZnSe/$MoSe_2$@C	PMA/ZIF-8	Self-assembly, calcination and selenization	Removal of excess organic solvent molecule	18
Nanocomposite confined in a hollow sphere	$NiCo_2(S_xSe_{1-x})_5$/graphitic carbon	NiCo-MOF microsphere	Hydrothermal treatment, calcination and sulfidation/selenization	Solid-state decomposition	60
Hollow polyhedron hybrid	NiCo-LDH/Co_9S_8 (LDH: layered double hydroxide)	ZIF-67	Annealing, hydrothermal treatment and sulfurization	Calcination treatment	61
Hierarchical core–shell nanocubes with hollow structure	CoS_2/C@SnS_2	Co-MOF nanocube	Hydrothermal treatment	Anion exchange	11
Hollow sandwich structure	C–MoS_2–C	Gibbsite	Hydrothermal and calcination	Etching with HCl	62
Sandwich-like three-layered hierarchical nanotube	TiO_2@C@MoS_2	MnO_2 nanowire	Annealing, hydrothermal treatment and etching	Acid etching	63
Cluster in a nanotube	Na_2Se@SWCNT	—	Theoretical study	—	64
Peapod-like nanowire	CoS⊂C, CoSe⊂C	Cobalt-nitrilotriacetic acid nanowire	Hydrothermal, annealing and sulfuration	Porous carbon	38
Bamboo-like hollow tube	MoS_2/N-doped C	MoS_2/oleylamine tube	Hydrothermal and sulfuration	Self-assembly of tube in the mixed solvent (ethanol/water)	65
NPs encapsulated in a nanotube	$Fe_{1-x}S$@C nanotubes	—	*In situ* solid-state approach, including pyrolysis and sulfidation	Vapor–liquid–solid mechanism	40
NPs encapsulated in a nanotube	Fe–S@CNTs	Carbon nanotube	Vapor deposition	—	19
NPs encapsulated in a nanotube	FeS_2@C nanotube	Carbon nanotube	Annealing and sulfidation	—	66
Nanotube composite	MoS_2@C	$Mo_3O_{10}(C_2H_{10}N_2)$ nanowire	Hydrothermal treatment sulfuration and carbonization	Kirkendall effect	23
Interlaced nanotube threaded hollow nanobox	Co_3S_4–C	Carbon nanotubes/ZF-67	Solvothermal sulfuration and thermal annealing	Kirkendall effect	46
Confined NPs on a carbon nanotube network	CNT/CoS@C	—	Sulfidation and carbonization	Dissolution–recrystallization and Ostwald ripening	67
Hollow hybrid	SnO_2/SnS_2	SnO_2 hollow sphere	Two-step hydrothermal treatment	—	68
Hybrid hollow architecture	ZnS nanorods rooted in the porous carbon polyhedron	ZIF-8 polyhedron	Sulfidation and carbonization	Solid-state decomposition	69
Hollow nanosphere assembled from ultrathin NSs	$NiCo_2S_4$@C	SiO_2	Hydrothermal treatment, calcination, sulfidation and etching	Etching with OH^- released from the hydrolysis of sulfide ions	49

This journal is © The Royal Society of Chemistry 2020

Open Access Article. Published on 26 December 2019. Downloaded on 2/19/2026 12:47:17 PM.
This article is licensed under a Creative Commons Attribution-NonCommercial 3.0 Unported Licence.

Table 1 (*Contd.*)

Types of materials	Component	Template	Synthesis route	Interior void formation principle	Reference
Sponge-like composite	(Co_9S_8 quantum dots@hollow carbon polyhedral)@rGO	ZIF-67@GO	Thermal reduction, carbonization, and sulfidation	Carbonization of the organic ligands	48
Hollow sphere	S/C	SiO_2	Hydrothermal treatment, ball milling, carbonization and etching	Etching with HF	70
Hollow hybrid	Hollow CoS@porous carbon polyhedral/carbon nanotube	Co-based ZIF-67 template	Annealing and sulfidation	*In situ* carbonization	71
Hollow prism	M-MoS_3 (M: Co, Ni)	M acetate hydroxide prism, Co-glycerate sphere, and ZIF-67 polyhedron	Precipitation, annealing	Outward flow of M^{2+} consuming the core template	72
Nanodots in a porous nanowire	FeS nanodots⊂porous graphitic carbon nanowire	—	Electrospinning technique, annealing and hydrothermal treatment	Graphitization of the amorphous carbon resulting in the formation of pores	73
Composite encapsulated in a hollow cube	$NiCo_2S_4$@nitrogen-doped carbon cube	$Ni_3[Co(CN)_6]_2$@polydopamine nanocube	Self-polymerization, pyrolysis and vulcanization	—	74
Pistachio-shuck-like core/shell nanostructure	$MoSe_2$/C	—	Reaction under high temperature and inert atmosphere	—	3
"Ship in a bottle" nanostructure	CoS_2/C	Ketjen Black EC600JD carbon	Co^{2+} impregnation	—	75

realized, placing great pressure on the vehicles' battery packs.[80] Therefore, advanced multiple-electron anode materials with high energy density, rate capacity and cycling stability are called for and in urgent demand.

Among diverse alternatives, including MCs, metal oxides, Li-alloys (Si, Sn, Ge, Sb), *etc.*, MCs are extraordinarily appealing because of their similar layered structure to graphite but superior capacity. For example, MoS_2, a representative two-dimensional (2D) layer material, has a higher theoretical capacity of 669 mA h g^{-1}. Nevertheless, the practical applications of these MCs are still hampered by the huge volume expansion and contraction during lithiation and delithiation processes, which will subsequently lead to (1) the pulverization and run away of the active component; (2) loss of electrical contact between the active component and conductive matrix; (3) production of a thick and insulating solid electrolyte interphase (SEI). Consequently, rapid capacity fading occurs for these anode materials. Besides, the limited electrical conductivity of MCs also blocks their further progress.

The rational engineering of advanced CHMCs is one possible solution to circumvent these issues (Fig. 15). For example, Lou's group developed a confined nanobox with a CoSe-enriched inner shell and an amorphous carbon-enriched outer shell (CoSe@carbon), using a template-assisted strategy.[54] When evaluated as anode materials for LIBs, these unique CoSe@carbon nanoboxes manifest decent lithium-storage performance in terms of high specific capacity, exceptional rate capability, and excellent cycling stability (Fig. 16a–c). Moreover, this confined nanobox shows a high initial coulombic efficiency of 78.3% with small irreversible capacity loss during the first discharge/charge cycle. Such superiority mainly arises from the confined hollow architecture of the CoSe@carbon nanoboxes, *i.e.*, their hollow interior can relieve the stress produced from CoSe-involved conversion reactions during continuous lithiation/delithiation processes, while the carbon-enriched outer shell can effectively protect the CoSe NPs from pulverization/shedding, and meanwhile, the carbon matrix can serve as highways for facile and rapid charge transport, thus ensuring effective lithium insertion/extraction even at high current densities.

Functionalizing the carbon shell with plenty of pores can further promote the transport of charge/Li^+, contributing to preeminent lithium storage performances. For the yolk–shell structured MoS_2@C anode with petal-like MoS_2 NSs confined within the cavity of hollow mesoporous carbon spheres,[41] besides enhancing the electrical conductivity/structural stability of MoS_2@C, the CHMCs are also helpful in accelerating the permeation of the electrolyte/reactant inside the HMCSs *via* their mesoporous shell, thus bringing about sufficient contact between the electrode material and electrolyte/reactant for fast Li^+ diffusion and migration. Consequently, a commendable reversible capacity of 993 mA h g^{-1} at 1 A g^{-1} after 200 cycles, a rate capability of 595 mA h g^{-1} at 10 A g^{-1}, and long-term cycle durability (962 mA h g^{-1} at 1 A g^{-1} after 1000 cycles and 624 mA h g^{-1} at 5 A g^{-1} after 400 cycles) are achieved for LIBs (Fig. 16d–g), outperforming the pure

Open Access Article. Published on 26 December 2019. Downloaded on 2/19/2026 12:47:17 PM.
This article is licensed under a Creative Commons Attribution-NonCommercial 3.0 Unported Licence.

MoS_2 and C@MoS_2 counterparts. Additionally, Tu and co-workers constructed a hierarchical microsphere assembly (MoS_2/C) comprised of interconnected MoS_2 NSs and a thin carbon outer layer by means of a template-free strategy.[24] The NSs herein are self-assembled to form microspheres, thus producing abundant holes between each other, which can also serve as electrolyte/ion/electron transfer paths for brilliant capacity and rate capability. Besides, the wrapped carbon shell contributes to the enhancement of both the electrical conductivity and structural stability of the whole assembly. By virtue of these structural characteristics, the MoS_2/C microspheres display preeminent Li/Na-ion storage bifunctionality (Fig. 17), including superior capacity (Li^+: 1017 mA h g^{-1} at 100 mA g^{-1} and Na^+: 531 mA h g^{-1} at 100 mA g^{-1}), rate capability (Li^+: 434 mA h g^{-1} at 1 A g^{-1} and Na^+: 102 mA h g^{-1} at 1 A g^{-1}), and cycling stability (Li^+: 902 mA h g^{-1} after 200 cycles and Na^+: 342 mA h g^{-1} over 100 cycles).

Lithium–sulfur batteries. As a promising alternative to LIBs, lithium–sulfur (Li–S) batteries possess several advantages, such as a high theoretical specific capacity of around 1675 mA h g^{-1} and an energy density of about 2600 W h kg^{-1}, both of which are superior to those of the LIBs (specific capacity of about 150 mA h g^{-1} and energy density of approximately 420 W h kg^{-1}).[17] Moreover, the $LiCoO_2$ cathode of LIBs is expensive (~$20 kg^{-1}) and toxic, while the S cathode of Li–S batteries has abundant earth reserves as well as low cost ($0.05 kg^{-1}) and toxicity.[52,81] These virtues make Li–S batteries a competitive candidate for next-generation energy storage systems. Nevertheless, the performances of Li–S batteries are still precluded by several obstacles: (1) large volume expansion of the sulfur cathode during the lithiation (discharge) process; (2) low conductivity of sulfur and lithium sulfides; (3) the generation of the lithium polysulfide (LiPS) intermediate (Li_2S_n, $n \geq 4$) during the reduction of S, which is easily dissolved and shuttled to the anode, leading to rapid decay of capacity and low coulombic efficiency.[82] Therefore, new materials and ingenious construction are required to tackle these problems.

Cui's group reported the use of polarized metal sulfides (TiS_2) to bind Li_2S/Li_2S_n species,[83] and improved electrochemical behaviour is realized thanks to the strong binding strength between TiS_2 and LiPS species (the calculated binding energy between Li_2S and single-layer TiS_2 is 2.99 eV, which is 10 times higher than that between Li_2S and single-layer graphene) and the high conductivity of TiS_2. In spite of this, the resultant life span is still unsatisfactory owing to the pronounced volume change under continuous cycling.

Restricting the LiPS species in confined hollow nanostructures (with the property of polarization) which have chemical interactions with the LIPS is an ingenious strategy to prevent the LiPS from losing and shuttling because it can serve as a reservoir for buffering the volume variation of the sulfur cathode during the repeated lithiation and delithiation process.[84] So far, the reported materials mainly include modified carbon materials, polymers and some inorganic materials, among which MCs have shown attractive effects.[84] For example, Jin and Liu's group prepared an efficient sulfur host material with hollow Co_3S_4 nanoboxes interconnected by carbon

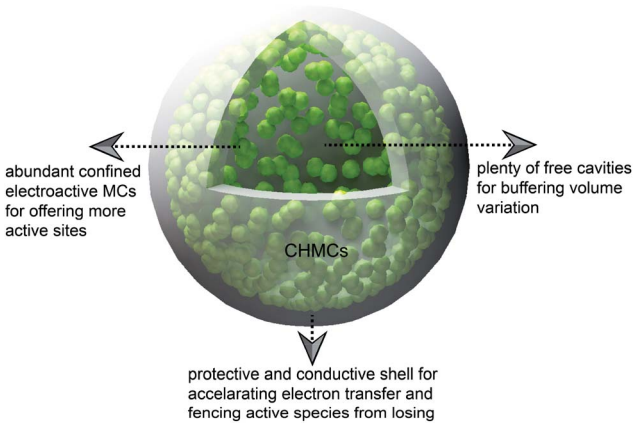

Fig. 15 Schematic illustration of the relationship between the structural features of CHMCs and their energy storage performances.

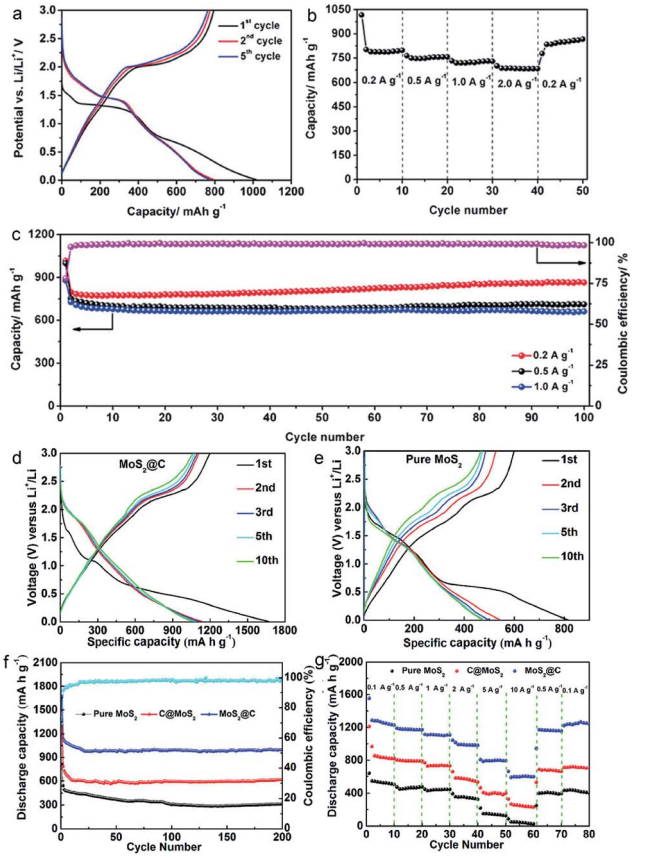

Fig. 16 (a) Discharge/charge voltage profiles at 0.2 A g^{-1}, (b) rate performance at current densities ranging from 0.2 to 2.0 A g^{-1}, and (c) cycling performance at 0.2, 0.5, and 1.0 A g^{-1} and the coulombic efficiency at 0.2 A g^{-1} for CoSe@carbon nanoboxes. Reproduced from ref. 54, with permission from Wiley, 2016. Charge/discharge voltage profiles of the (d) MoS_2@C and (e) pure MoS_2 at 1 A g^{-1}. (f) Cycling performance of pure MoS_2, C@MoS_2, and MoS_2@C nanospheres and coulombic efficiency of MoS_2@C nanospheres at 1 A g^{-1}. (g) Cycling performance at various current densities (0.1 to 10 A g^{-1}). Reproduced from ref. 41, with permission from American Chemical Society, 2017.

This journal is © The Royal Society of Chemistry 2020

Open Access Article. Published on 26 December 2019. Downloaded on 2/19/2026 12:47:17 PM.
This article is licensed under a Creative Commons Attribution-NonCommercial 3.0 Unported Licence.

nanotubes (denoted as CNTs/Co_3S_4-NBs) by a self-templating approach.[46] In this composite material, the Co_3S_4-NBs work well in arresting and storing the LiPS in their cavities *via* chemical bonding (due to the polar feature of the Co_3S_4-NBs) and structural confinement effects. Meanwhile, the 3D CNT network enhances the charge transfer properties of the whole framework (the carbon in Li–S batteries is mainly responsible for enhanced electrical conductivity rather than bonding the LIPS due to its nonpolar nature). As a result, this S@CNTs/Co_3S_4-NB cathode presents superior reversible capacity (a high initial discharge capacity of 1535 mA h g^{-1} and remains at 1254 mA h g^{-1} after 100 cycles), rate performance (discharge capacities of 1330, 1165, 988, 859, and 702 mA h g^{-1} at 0.2, 0.5, 1.0, 2.0, and 5.0C, respectively), and long cycling stability (a capacity decay of 0.042% per cycle at 1.0C and 0.068% per cycle at 2.0C for 500 cycles), exceeding the S@Co_3S_4-NB and S@CNT counterparts (Fig. 18). Besides, Qiao and Wang's group developed another sulfur host material with nanosized NiS uniformly distributed on carbon hollow spheres (S/NiS@C-HS) using an *in situ* thermal reduction and post sulfidation method.[21] The NiS in S/NiS@C-HS has a high affinity for the polysulfides *via* chemical interactions while the C-HS can act as both the physical confinement pocket for polysulfide storage and 3D highway for rapid electron transfer. Moreover, the NiS core has strong chemical coupling with the C-HS shell, which favors fast charge transfer and redox kinetics of the sulfur cathode. Consequently, this composite material delivers a capacity decay as low as 0.013% per cycle and a capacity of 695 mA h g^{-1} at 0.5C after 300 cycles at a high sulfur loading of 2.3 mg cm^{-2} (Fig. 19).

Beyond confinement, the utilization of the soluble characteristic of LIPS is also certified to be an effective method for enhanced Li–S batteries behaviors. This is achieved based on the dynamic precipitation and dissolution equilibrium of LiPS when extra polysulfides are added into the electrolyte.[84] For instance, Peng *et al.* took advantage of high concentration polysulfides as extrinsic healing agents to homogenize the distribution of polysulfides.[85] In detail, in the absence of extrinsic polysulfides, the test-generated polysulfides would lead to LiPS with inhomogeneous distribution and thus uneven precipitates. Differently, if high concentration of polysulfide is pre-existed in the electrolyte, the dramatic variation in polysulfides distribution would be mitigated, contributing to relatively homogeneous distributed polysulfides. This would facilitate the mediation of phase transfer, and finally lead to decent Li–S battery properties. Overall, benefiting from the self-healing function of LiPS, Li–S batteries can realize rapid kinetics, higher discharge capacity and stable cycling performance. It is worth mentioning that apart from polysulfides, other additives, such as $LiNO_3$ [86] and P_2S_5 [87] can also offer admirable Li–S battery performance. Considering that the

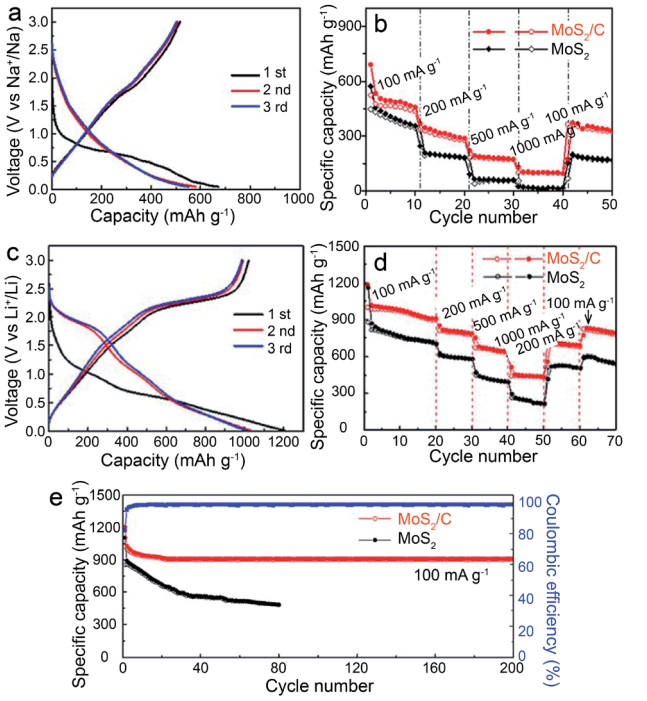

Fig. 17 (a) Charge/discharge profiles at 100 mA g^{-1}, and (b) rate performance from 100 mA g^{-1} to 1000 mA g^{-1} for MoS_2/C electrodes in SIBs. (c) Charge/discharge profiles at 100 mA g^{-1}, (d) rate performance from 100 mA g^{-1} to 1000 mA g^{-1}, and (e) cycling performance at 100 mA g^{-1} for MoS_2/C electrodes in LIBs. Reproduced from ref. 24, with permission from Wiley, 2018.

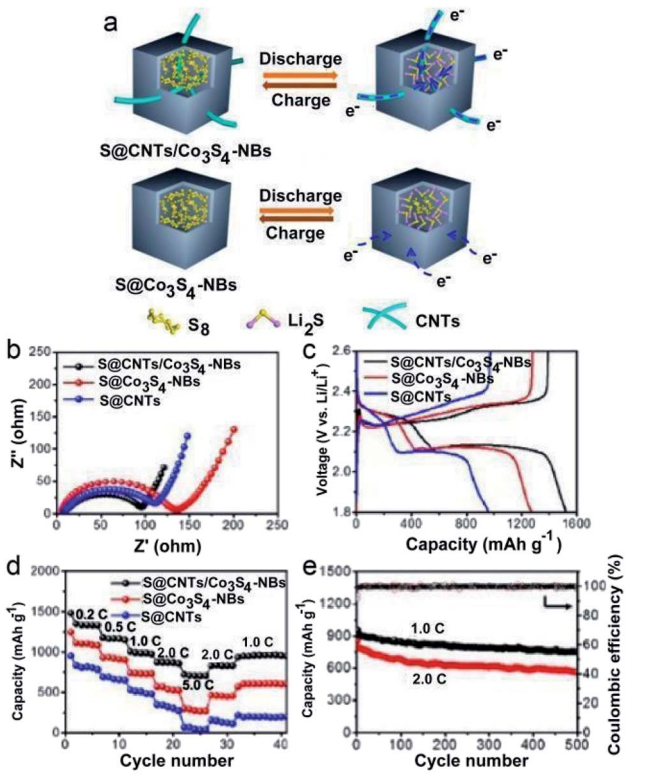

Fig. 18 (a) Structural advantages of the S@CNTs/Co_3S_4-NB cathode over the S@Co_3S_4-NB cathode during charge–discharge processes. (b) EIS curves, (c) galvanostatic charge–discharge voltage profiles at 0.2C and (d) rate capabilities of the S@CNTs/Co_3S_4-NB, S@Co_3S_4-NB and S@CNT electrodes. (e) Long-term cycle performances of the S@CNTs/Co_3S_4-NB electrode at 1.0 and 2.0C. Reproduced from ref. 46, with permission from American Chemical Society, 2017.

Open Access Article. Published on 26 December 2019. Downloaded on 2/19/2026 12:47:17 PM.
This article is licensed under a Creative Commons Attribution-NonCommercial 3.0 Unported Licence.

theme of this review is confined hollow structures, details of these additives are not discussed herein.

Sodium-ion batteries. Although LIBs have shown high energy density, long life span and commendable applications in our daily lives, the insufficient reserves and of Li resources in the earth's crust and its high cost largely hinder their development for large-scale energy storage purposes.[88,89] Under this circumstance, sodium-ion batteries (SIBs) are considered as a potential alternative to the prevailing LIBs, due to the natural abundance of sodium (*ca.* 2.6% in the Earth's crust).[90,91] Nevertheless, SIBs still face some challenges: (1) SIBs have lower power and energy densities than LIBs as Na has a larger ionic size (0.102 nm > 0.076 nm) and lower standard electrochemical potential (2.71 V < 3.04 V) than Li; (2) lithium can exist in octahedral or tetrahedral coordination, but sodium prefers octahedral and prismatic coordination.[29,90,92] This may cause a sluggish reaction mechanism and critical conditions for sodium-ion diffusion, which means that some electrode materials appropriate for LIBs may not be suitable for SIBs. For example, graphite, a commercial adopted anode material for LIBs, does not function in SIBs because Na will plate on the carbon surface before forming graphite intercalation compounds, leading to low capacity (lower than 35 mA h g^{-1}) in carbon-ester electrolyte.[93] Therefore, the development of suitable anode materials is crucial for boosting SIBs, but still remains a challenge.

In attempts to mitigate these problems, the fabrication of CHMCs is of great importance due to their high theoretical specific capacity (such as TiS_2), good stability and rich interior space. Hence, more attempts have been made to explore appropriate CHMCs for SIBs. For example, tin disulfide (SnS_2) is regarded as a promising anode material for SIBs with high specific capacity, and unfolds great ability for Na^+ uptake and release. However, the low conductivity and large volume variation during reaction with Na^+ largely hinder its practical application.[20,94] To address this issue, our group has recently developed a series of advanced confined hollow structures, including SnS_2 NSs confined in hollow carbon nanotubes (SnS_2@CNBs), nanoboxes (SnS_2@CNBs) and carbon nanospheres (SnS_2@CNSs).[20] Delightedly, compared with the common SnS_2/C nanohybrids, these confined hollow structures all manifest superior sodium storage properties. Especially, SnS_2@CNSs exhibit the brightest performances with a specific capacity of about 634 mA h g^{-1} at 0.2 A g^{-1} and excellent rate capability of 410 mA h g^{-1} at 5 A g^{-1} (Fig. 20). Such superiority mainly originates from their unique structural advantages, *i.e.*, the thin carbon shell can enhance the electrical conductivity of the whole electrode, and protect the active SnS_2 component from aggregation, as well as buffering the volume expansion during cycling; besides, the ultrathin SnS_2 NSs with high surface area can facilitate Na^+ diffusion, leading to capacitance-dominated reactions and high rate performances.

Besides SnS_2 NSs, other confined nanostructures, such as MoS_2/C hierarchical hollow carbon nanospheres[56] and SnS@C nanotubes[59] also demonstrate glorious electrochemical performance for SIBs. For instance, Sun's group embedded $MoSe_2$ NSs within the cavities of hollow carbon nanospheres to form

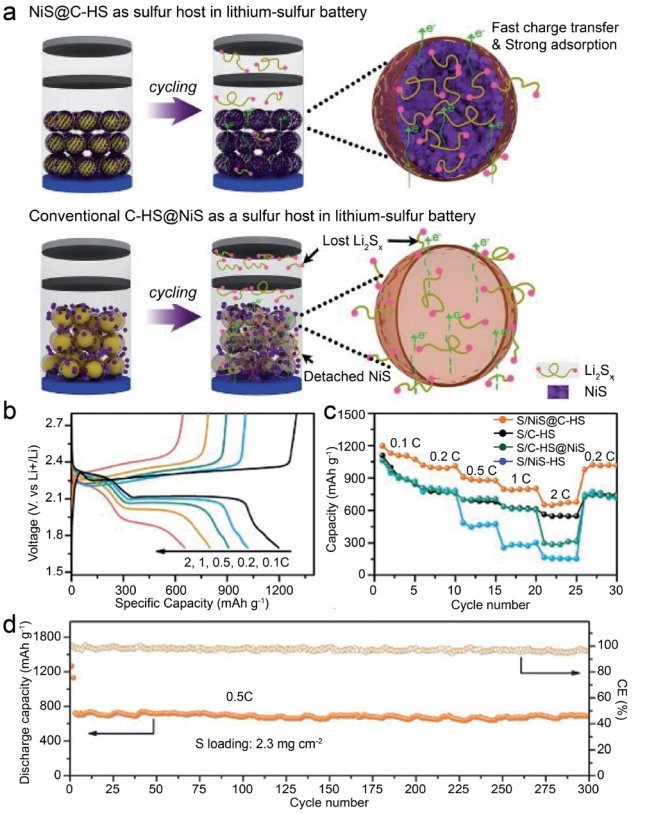

Fig. 19 (a) Schematic illustration of NiS@C-HS and C-HS@NiS as sulfur hosts for improving Li–S battery performances. (b) Discharge/charge curves of S/NiS@C-HS at different rates. (c) Rate capabilities of sulfur cathodes at 0.2C. (d) Cycling performances and CE of the S/NiS@C-HS at 0.5C. Reproduced from ref. 21, with permission from Wiley, 2017.

$MoSe_2$@HCNS construction.[43] The $MoSe_2$ herein displays few-layer crystal fringes (≤3) and expanded interlayer spacing (from 0.64 nm to 1.02 nm). Thanks to the expanded (002) crystal planes, 2D few-layer $MoSe_2$ NS structure, and unique carbon shell-stabilized framework, such $MoSe_2$@HCNS exhibits excellent cycling life with discharge capacities of 502 and 471 mA h g^{-1} over 1000 cycles at 1 and 3 A g^{-1}, respectively. It is noteworthy that the coulombic efficiencies of all the rate performances exceed 98.3%. On further raising the current density to 10 A g^{-1}, the capacity can remain at 382 mA h g^{-1}, and the capacity will recover to 532 mA h g^{-1} once the current density decreases to 1 A g^{-1} after 200 cycles. Therefore, the $MoSe_2$@HCNS displays great potential for application in SIBs.

Supercapacitors. Supercapacitors, also known as ultracapacitors or electrochemical capacitors, have attracted much attention during the past few decades, thanks to their remarkable power density, long lifespan (2–3 orders of magnitude longer than conventional rechargeable batteries) and eco-friendly features.[95] Based on the intrinsic energy storage mechanisms, supercapacitors can be classified into electrical double layer capacitors (EDLCs) and pseudocapacitors. EDLCs feature electrostatic ion adsorption at the electrode–electrolyte interface, while pseudocapacitance originates from the fast and

 This journal is © The Royal Society of Chemistry 2020

Open Access Article. Published on 26 December 2019. Downloaded on 2/19/2026 12:47:17 PM.
This article is licensed under a Creative Commons Attribution-NonCommercial 3.0 Unported Licence.

reversible faradaic redox reactions. Compared with EDLCs, pseudocapacitors deliver larger specific capacitance and energy density, and thus are considered especially promising for the next generation of electrochemical capacitors.[96] To boost their progress, highly efficient electrode materials with short electron/ion transport pathways and abundant electroactive sites are desired, yet of great significance.

Nanostructured MCs confined in hollow cavities possess a large specific surface area providing abundant reaction sites, vast free space for rapid transport of electrolyte, and importantly, 3D construction for inhibiting the restacking of nanosized MCs, which characteristics make them attractive for pseudocapacitor devices and some progress has been made. For example, Lou *et al.* developed a double-shelled rhombic dodecahedral cage (RDCs) of zinc–cobalt sulfide (Zn-Co-S) *via* a sequential chemical etching and sulfurization strategy.[34] Benefiting from their unique structural and compositional advantages, this double-shelled Zn-Co-S RDC demonstrates superior hybrid supercapacitor behaviors with a specific capacitance of 1266 F g^{-1} at 1 A g^{-1} and long-term cycling stability (91% retention over 10 000 cycles). By comparison, single-shelled Zn-Co-S RDCs exhibit much lower capacitance. This emphasizes the advantages of double-shelled confinement nanostructures that are capable of containing a higher weight fraction of active species and improving the electric contact. Besides Zn-Co-S RDCs, other double-shelled metal sulfides, such as hierarchical NiS box-in-box hollow structure,[33] also exhibit high specific capacitance (668 F g^{-1} at 1 A g^{-1}), excellent rate capability (71% capacitance retention at 20 A g^{-1}), and good cycling stability (retention of 93.4% after 3000 cycles at 4 A g^{-1}), signifying the superiority of double-shelled confined structures.

Additionally, the carbon-coated confined structure is also efficient for enhanced supercapacitor performances. As an example, by taking advantage of the intrinsic and intended features of the NiS-NC HS comprising the N-doped carbon (NC) hollow shell and NiS core,[35] the constructed core–shell structure effectively avoids the agglomeration of the neighboring NiS particles and the NiS dissolution or side reactions, thus showing an excellent specific capacitance of 1170.72 F g^{-1} (at 0.5 A g^{-1}), C_s value of 260.03 F g^{-1} (at 0.5 A g^{-1}) and stability (capacitance retention of 90.71% at 6 A g^{-1} after 4000 cycles) (Fig. 21). Besides, Lu's group developed a novel nanoplate-shaped electrode material with 2D layered MoS_2 flakes confined within the hollow interlayer of hexagonal graphitic carbon platelets by a hydrothermal method followed by calcination and etching.[77] The obtained sandwich-like assemblies, carbon–MoS_2–carbon, show a high specific surface area of 543 m^2 g^{-1} and pore size of about 5.3 nm. The hollow structure ensures plenty of well-defined interior voids which can buffer the volume changes during the charging and discharging process. Moreover, benefiting from their hollow carbon shell, high electronic conductivity is realized. As a result, such particular confined hollow structure exhibits remarkable capacitive behavior with a high specific capacitance of 248 F g^{-1} (0.12 F cm^{-2}) at 0.1 A g^{-1} and decent stability over

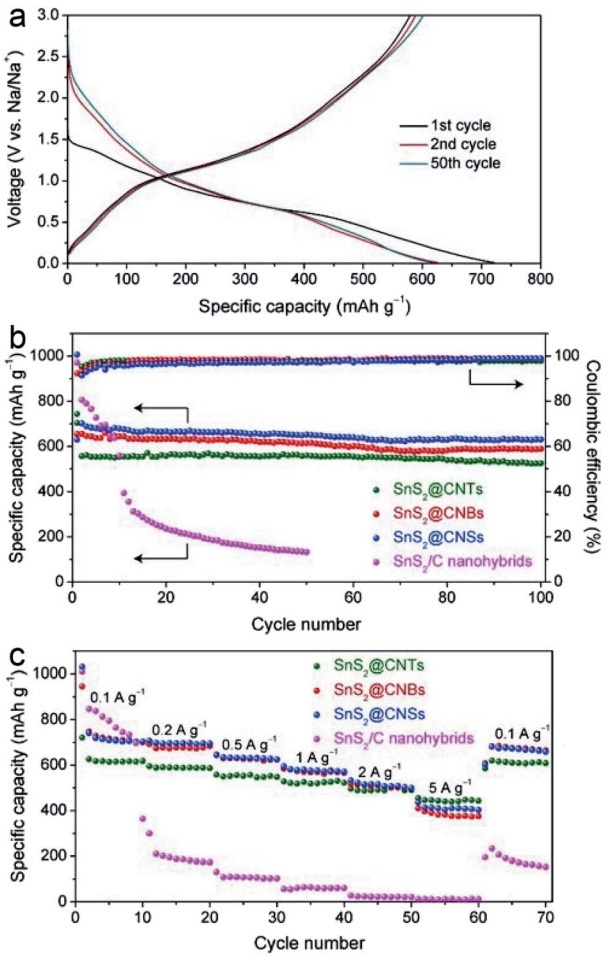

Fig. 20 (a) Charge–discharge voltage profiles of SnS_2@CNTs at 0.1 A g^{-1}. (b) Cycling performances and corresponding coulombic efficiencies of SnS_2@CNTs, SnS_2@CNBs, SnS_2@CNSs, and SnS_2/C nanohybrids at 0.2 A g^{-1}. (c) Rate capabilities of SnS_2@CNTs, SnS_2@CNBs, SnS_2@CNSs, and SnS_2/C nanohybrids. Reproduced from ref. 20, with permission from Elsevier, 2018.

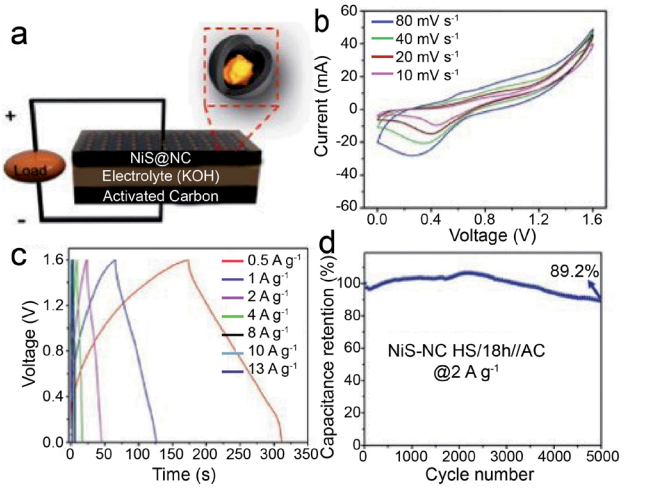

Fig. 21 (a) An illustration of the asymmetric NiS-NC HS/18 h//AC supercapacitor, (b) CV curves at different scan rates, (c) GCD curves at different current densities, and (d) cyclic performance of NiS-NC HS/18 h//AC at a current density of 2 A g^{-1}. Reproduced from ref. 35, with permission from Wiley, 2018.

Open Access Article. Published on 26 December 2019. Downloaded on 2/19/2026 12:47:17 PM.
This article is licensed under a Creative Commons Attribution-NonCommercial 3.0 Unported Licence.

Table 2 Energy storage performances of different CHMCs

Types of materials	Rate capability (mA g^{-1})	Specific capacity (mA g^{-1})	Stability	Application field	Reference
CuS@CoS_2 double-shelled nanobox	304 mA h g^{-1} at 5 A g^{-1}	625 mA h g^{-1} at 0.1 A g^{-1}	79% capacity retention at 0.5 A g^{-1} after 500 cycles	SIBs	7
Double-shelled Zn-Co-S rhombic dodecahedral cage	720 F g^{-1} at 20 A g^{-1}	1266 F g^{-1} at 1 A g^{-1}	91% capacity retention at 10 A g^{-1} after 10 000 cycles	Supercapacitor	34
CoS NPs/CoS NSs double-shelled hollow structure	585 F g^{-1} at 20 A g^{-1}	980 F g^{-1} at 1 A g^{-1}	89% capacity retention at 5 A g^{-1} after 10 000 cycles	Supercapacitor	6
MS (M: Ni, Cu, Mn) box-in-box hollow structure	NiS: 472 F g^{-1} at 20 A g^{-1}	NiS: 668 F g^{-1} at 1 A g^{-1}	Retention of 93.4% after 3000 cycles at 4 A g^{-1}	Supercapacitor	33
"Brain-coral-like" mesoporous CoS_2@N-doped carbon nanoshell	525.3 mA h g^{-1} at 2C	1300 mA h g^{-1} at 0.1C	903 mA h g^{-1} at 0.1C after 100 cycles	Li–S battery	52
Hollow Co_9S_8 NPs embedded in a carbon nanocage	278 mA h g^{-1} at 10C	536 mA h g^{-1} at 0.2C and	365 mA h g^{-1} at 1C after 150 cycles	Lithium-ion storage	51
FeS_2@C yolk–shell nanobox	403 mA h g^{-1} at 5 A g^{-1}	560 mA h g^{-1} at 0.1 A g^{-1}	330 mA h g^{-1} at 2 A g^{-1} after 800 cycles	SIBs	36
Metallic and polar Co_9S_8 inlaid carbon hollow nanopolyhedron	690 mA h g^{-1} at 3C	1160 mA h g^{-1} at 0.2C	560 mA h g^{-1} at 2C after 1000 cycles	Li–S battery	4
ZnSe@N-doped carbon	474 mA h g^{-1} at 12.8 A g^{-1}	1162 mA h g^{-1} at 0.2 A g^{-1}	1134 mA h g^{-1} at 0.6 A g^{-1} after 500 cycles	LIBs	53
SnS_2 NSs in a hollow carbon nanostructure	SnS_2@hollow carbon nanospheres: 517 mA h g^{-1} at 2 A g^{-1}	709 mA h g^{-1} at 0.1 A g^{-1}	631 mA h g^{-1} at 0.2 A g^{-1} after 100 cycles	SIBs	20
$MoSe_2$ NSs confined in a hollow carbon nanosphere	382 mA h g^{-1} at 10 A g^{-1}	562 mA h g^{-1} at 1 A g^{-1}	501 and 471 mA h g^{-1} at 1 and 3 A g^{-1} after 1000 cycles	SIBs	43
SnS nanosheet @hollow mesoporous carbon sphere-reduced graphene oxide	LIBs: 230 mA h g^{-1} at 3.2 A g^{-1}; SIBs: 336 mA h g^{-1} at 1.6 A g^{-1}	LIBs: 1362 mA h g^{-1} at 0.2 A g^{-1}; SIBs: 825 mA h g^{-1} at 0.2 A g^{-1}	LIBs: 1027 mA h g^{-1} at 0.2 A g^{-1} after 100 cycles. SIBs: 445 mA h g^{-1} at 0.1 A g^{-1} after 100 cycles	LIBs and SIBs	47
FeS_2 NSs encapsulated in a 3D porous carbon sphere	453.6 mA h g^{-1} at 2 A g^{-1}	514.9 mA h g^{-1} at 0.5 A g^{-1}	272.4 mA h g^{-1} at 5 A g^{-1} after 500 cycles	SIBs	37
Petal-like MoS_2 NSs confined in a mesoporous carbon sphere	595 mA h g^{-1} at 10 A g^{-1}	1280 mA h g^{-1} at 0.1 A g^{-1}	962 mA h g^{-1} at 1 A g^{-1} after 1000 cycles	LIBs	41
Bullet-like Cu_9S_5@nitrogen-doped carbon hollow structure	237 mA h g^{-1} at 5 A g^{-1}	385 mA h g^{-1} at 0.3 A g^{-1}	79% capacity retention at 2 A g^{-1} after 4000 cycles	SIBs	22
CoSe@carbon nanobox	686 mA h g^{-1} at 2.0 A g^{-1}	787 mA h g^{-1} at 0.2 A g^{-1}	94.5% (711 mA h g^{-1}) of the 2nd cycle discharge capacity retention at 0.5 A g^{-1} in the 100th cycle	LIBs	54
NiS core–nitrogen-doped carbon hollow shell structure	843.75 F g^{-1} at 10 A g^{-1}	1170.72 F g^{-1} at 0.5 A g^{-1}	90.71% capacitance retention at 6 A g^{-1} after 4000 cycles	Supercapacitor	35
Coconut-like monocrystalline SnS/C nanosphere	557 mA h g^{-1} at 5 A g^{-1}	936 mA h g^{-1} at 0.1 A g^{-1}	936 mA h g^{-1} at 0.1 A g^{-1} for 50 cycles and 830 mA h g^{-1} at 0.5 A g^{-1} for another 250 cycles	LIBs	55
Coupled carbon NSs/MoS_2 nanocrystal hierarchical hollow nanosphere	262.7 mA h g^{-1} at 8 A g^{-1}	574.7 mA h g^{-1} at 0.2 A g^{-1}	410 mA h g^{-1} at 4 A g^{-1} after 1000 cycles	SIBs	56
Pistachio-shuck-like $MoSe_2$/C core/shell nanostructure	224 mA h g^{-1} at 2.0 A g^{-1}	382 mA h g^{-1} at 0.2 A g^{-1}	226 mA h g^{-1} at 1 A g^{-1} over 1000 cycles	Potassium-ion battery	3
WS_2 NSs vertically embedded in hollow mesoporous carbon	396 mA h g^{-1} at 10 A g^{-1}	935 mA h g^{-1} at 0.1 A g^{-1}	784 mA h g^{-1} at 1 A g^{-1} after 1000 cycles	LIBs	42
Hierarchical Co_9S_8@carbon hollow microsphere	411 mA h g^{-1} at 5 A g^{-1}	614 mA h g^{-1} at 0.1 A g^{-1}	223 mA h g^{-1} at 5 A g^{-1} after 10 000 cycles	SIBs	44

This journal is © The Royal Society of Chemistry 2020

Open Access Article. Published on 26 December 2019. Downloaded on 2/19/2026 12:47:17 PM.
This article is licensed under a Creative Commons Attribution-NonCommercial 3.0 Unported Licence.

Table 2 (*Contd.*)

Types of materials	Rate capability (mA g^{-1})	Specific capacity (mA g^{-1})	Stability	Application field	Reference
3D hybrid of NiS and hollow carbon spheres	674 mA h g^{-1} at 2C	1196 mA h g^{-1} at 0.1C	695 mA h g^{-1} at 0.5C after 300 cycles	Li–S battery	21
Carbon-coated 3D porous interconnected SnS	Lithium storage: 329 mA h g^{-1} at 10 A g^{-1}; SIBs: 145 mA h g^{-1} at 10 A g^{-1}	Lithium storage: 953 mA h g^{-1} at 0.1 A g^{-1}; SIBs: 419 mA h g^{-1} at 0.1 A g^{-1}	80% capacity retention after 300 cycles (lithium storage: 535 mA h g^{-1} at 1 A g^{-1}; SIBs: 266 mA h g^{-1} at 1 A g^{-1})	LIBs and SIBs	57
Hierarchical nanotubes constructed by SnS NSs@C	290 mA h g^{-1} at 5 A g^{-1}	440 mA h g^{-1} at 0.2 A g^{-1}	440 mA h g^{-1} at 0.2 A g^{-1} after 100 cycles	SIBs	59
$MoSe_2$ confined within a ZnSe–C hollow porous sphere	Lithium storage: 363 mA h g^{-1} at 2 A g^{-1}; SIBs: 328 mA h g^{-1} at 4 A g^{-1}	Lithium storage: 1051 mA h g^{-1} at 0.2 A g^{-1}; SIBs: 468 mA h g^{-1} at 0.2 A g^{-1}	Lithium storage: 524 mA h g^{-1} at 4 A g^{-1} after 600 cycles; SIBs: 381 mA h g^{-1} at 4 A g^{-1} after 250 cycles	LIBs and SIBs	18
$NiCo_2(S_xSe_{1-x})_5$/graphitic carbon	Pseudocapacitors: 440.1C g^{-1} at 20 A g^{-1}. LIBs: 348.7 mA h g^{-1} at 5 A g^{-1}	Pseudocapacitors: 560.7C g^{-1} at 1 A g^{-1}; LIBs: 906.1 mA h g^{-1} at 0.1 A g^{-1}	Pseudocapacitor 476.2C g^{-1} (93.7% capacity retention) at 6 A g^{-1} after 2000 cycles LIBs: 865.2 mA h g^{-1} at 0.2 A g^{-1} after 100 cycles	Pseudocapacitors and LIBs	60
NiCo-LDH/ Co_9S_8 (LDH: layered double hydroxide)	1025C g^{-1} at 20 A g^{-1}	1653C g^{-1} at 4 A g^{-1}	95.4% capacity retention after 3000 cycles	Pseudocapacitors	61
SnS_2 NSs coating on nanohollow CoS_2/C	About 400.1 mA h g^{-1} at 10 A g^{-1}	854.5 mA h g^{-1} at 0.1 A g^{-1}	400.1 mA h g^{-1} at 10 A g^{-1} after 3500 cycles	SIBs	11
Hexagonal carbon–MoS_2–carbon nanoplates with a hollow sandwich structure	178 F g^{-1} at 1 A g^{-1}	248 F g^{-1} at 0.1 A g^{-1}	85% capacity retention at 1 A g^{-1} after 3000 cycles	Supercapacitor	62
Sandwich-like hierarchical TiO_2@carbon@MoS_2 tubular nanostructure	612 mA h g^{-1} at 2 A g^{-1}	925 mA h g^{-1} at 0.1 A g^{-1}	590 mA h g^{-1} at 1 A g^{-1} after 200 cycles	LIBs	63
Na_2Se confined within a single-walled carbon nanotube			Theoretical investigation	Sodium–selenium battery	64
Bamboo-like hollow tubes with a MoS_2/N-doped-C interface	131 mA h g^{-1} at 2 A g^{-1}	330 mA h g^{-1} at 0.05 A g^{-1}	151 mA h g^{-1} at 0.5 A g^{-1} after 1000 cycles	Potassium-ion battery	65
$Fe_{1-x}S$ encapsulated in a carbon nanotube	326.3 mA h g^{-1} at 8 A g^{-1}	492.7 mA h g^{-1} at 0.2 A g^{-1}	449.2 mA h g^{-1} at 0.5 A g^{-1} after 200 cycles	SIBs	40
Carbon nanotubes filled with Fe–S NPs	348 mA h g^{-1} at 2 A g^{-1}	698 mA h g^{-1} at 0.05 A h^{-1}	670 mA h g^{-1} at 0.05 A g^{-1} after 65 cycles	LIBs	19
FeS_2 NPs encapsulated in a carbon nanotube	345 mA h g^{-1} at 5 A g^{-1}	800 mA h g^{-1} at 0.2 A g^{-1}	525 mA h g^{-1} at 2 A g^{-1} after 1000 cycles	LIBs	66
Peapod-like carbon-encapsulated CoS or CoSe nanowire	CoS: 235 mA h g^{-1} at 5 A g^{-1} CoSe: 241 mA h g^{-1} at 5 A g^{-1}	CoS: 379 mA h g^{-1} at 0.1 A g^{-1} CoSe: 350 mA h g^{-1} at 0.1 A g^{-1}	CoS: 294 mA h g^{-1} at 0.1 A g^{-1} after 100 cycles CoSe: 299 mA h g^{-1} at 0.1 A g^{-1} after 100 cycles	SIBs	38
MoS_2@C nanotube	LIBs: 850 mA h g^{-1} at 5C; SIBs: 370 mA h g^{-1} at 5C	LIBs: 1326.9 mA h g^{-1} at 0.1C; SIBs: 610 mA h g^{-1} at 0.1C	LIBs: 1058.4 mA h g^{-1} (90% capacity retention) at 0.5C after 300 cycles. SIBs: 480 mA h g^{-1} at 0.5C after 200 cycles.	LIBs and SIBs	23
Interlaced carbon nanotube threaded hollow Co_3S_4 nanobox	702 mA h g^{-1} at 5C	1254 mA h g^{-1} at 0.2C	752 mA h g^{-1} at 1C after 500 cycles	Li–S battery	46
CNT/CoS@C	276 mA h g^{-1} at 5 A g^{-1}	562 mA h g^{-1} at 0.1 A g^{-1}	398 mA h g^{-1} at 0.5 mA g^{-1} after 200 cycles	SIBs	67

Open Access Article. Published on 26 December 2019. Downloaded on 2/19/2026 12:47:17 PM.
This article is licensed under a Creative Commons Attribution-NonCommercial 3.0 Unported Licence.

Table 2 (*Contd.*)

Types of materials	Rate capability (mA g^{-1})	Specific capacity (mA g^{-1})	Stability	Application field	Reference
Hollow SnO_2/SnS_2 hybrid	245.4 mA h g^{-1} at 2.5 A g^{-1}	497.8 mA h g^{-1} at 0.3 A g^{-1}	485.6 mA h g^{-1} at 0.3 A g^{-1} after 100 cycles	SIBs	68
ZnS nanorods rooted in the porous carbon polyhedron	608 mA h g^{-1} at 1.6 A g^{-1}	1388 mA h g^{-1} at 0.1 A g^{-1}	840 mA h g^{-1} at 0.6 A g^{-1} after 300 cycles	LIBs	69
Hollow nanospheres assembled from $NiCo_2S_4$@C NSs	700 mA h g^{-1} at 3.2 A g^{-1}	1592 mA h g^{-1} at 0.5 A g^{-1}	1178 mA h g^{-1} at 0.5 A g^{-1} after 200 cycles	LIBs	49
(Co_9S_8 quantum dots@hollow carbon polyhedral)@rGO	330 mA h g^{-1} at 6.4 A g^{-1}	738 mA h g^{-1} at 0.2 A g^{-1}	628 mA h g^{-1} at 0.3 A g^{-1} after 500 cycles	SIBs	48
Sulfur-grafted hollow carbon sphere	110 mA h g^{-1} at 5 A g^{-1}	581 mA h g^{-1} at 0.025 A g^{-1}	93% capacity retention from the 5th to 1000th cycles at 3 A g^{-1}	Potassium-ion batteries	70
Nitrogen-doped double-shelled hollow carbon spheres-sulfur hybrid	600 mA h g^{-1} at 2C	1360 mA h g^{-1} at 0.2C	940 mA h g^{-1} at 0.2C after 100 cycles	Li–S battery	17
CoS embedded within porous carbon polyhedral/carbon nanotubes	752 mA h g^{-1} at 10 A g^{-1}	1668 mA h g^{-1} at 0.2 A g^{-1}	1668 mA h g^{-1} at 0.2 A g^{-1} after 100 cycles	LIBs	71
FeS nanodots⊂ porous graphitic carbon nanowires	322 mA h g^{-1} at 10C	579 mA h g^{-1} at 0.1C	400 mA h g^{-1} at 0.5C after 50 cycles	LIBs	73
$NiCo_2S_4$ encapsulated in a hollow nitrogen-doped carbon cube	353 mA h g^{-1} at 1 A g^{-1}	480 mA h g^{-1} at 0.1 A g^{-1}	427 mA h g^{-1} at 0.5 A g^{-1} after 500 cycles	LIBs	74

3000 cycles for symmetric supercapacitor application. These performances are much superior to those of its hollow carbon counterpart, signifying that the superiority of the carbon–MoS_2–carbon nanoplate benefits from both the high electronic conductivity of the carbon shell and the intrinsic electrochemical activity of MoS_2 stuffing.

Table 2 summarizes the energy storage performances of different CHMCs, including rate capability, specific capacity, stability and application fields, which can serve as references and guide the fabrication of new-type CHMCs with enhanced energy storage performances.

Conclusions

In summary, we have reviewed the recent progress in the synthetic strategies of diverse CHMCs as well as their growth mechanisms. These CHMCs can be mainly classified into six categories, including double-shelled confined hollow structures with different shapes, core–shell confined structure with a hollow cavity, hierarchical NPs/NS-based confined structures encapsulated within different-shaped single-shelled hollow shells, and CHMCs with composite structures/components. Thanks to their unique structure features, including plenty of free cavities for buffering large volume variation, abundant electroactive MCs for offering more active sites and a protective carbon/MC shell for preventing active species from losing,[97] these CHMCs demonstrate admirable energy storage performances as electrode materials for LIBs, SIBs, Li–S batteries and supercapacitor systems. Although these studies provide massive advanced electrode materials which deepen our understanding of the link between confined hollow structure engineering and improved energy storage performance, there is still plenty of room for the further study of this research area. First, from the perspective of synthesis, precise control and fabrication of CHMCs through facile and large-scale synthesis methods are quite difficult. Further expanding the existing methods and developing new templates and strategies for complex confined structures would be very useful. Especially, the hollow structures will inevitably reduce the volumetric energy density of the electrodes because of the presence of interior cavities, so fine tuning the shell thickness and void size of the confined hollow structures is highly desirable in order to get a balance between high volumetric energy density and suitable void space for accommodating mechanical stress. Due to the difference in various energy storage systems, there are several issues, such as single-shell and multi-shell, shell composition, that need to be addressed toward rational design of confined hollow structures. Second, *in situ* electrochemistry studies combined with TEM, XPS and *etc.* need to be developed. The structural and chemical environment changes are usually accompanied by morphological and valence state changes that impact the electrochemical performances of materials. Therefore, various *in situ* techniques are of great potential in studying the microstructure transformation and ion diffusion at various length scales and high temporal resolution, offering important insights for designing structural and compositional modification strategies for improving system performance. Additionally, although

This journal is © The Royal Society of Chemistry 2020

Open Access Article. Published on 26 December 2019. Downloaded on 2/19/2026 12:47:17 PM.
This article is licensed under a Creative Commons Attribution-NonCommercial 3.0 Unported Licence.

theoretical calculation has been widely applied in electrochemical catalytic systems, there have been few reports on energy storage systems so far. The combination of experimental and theoretical calculation is expected to bring more possibilities in modulating the properties of CHMCs.

Conflicts of interest

There are no conflicts to declare.

Acknowledgements

This work was financially supported by the National Natural Science Foundation of China (21533012 and 21625502). The authors appreciate the financial support from the PAPD of Jiangsu Higher Education Institutions.

Notes and references

1 Y. Zhang, Q. Zhou, J. Zhu, Q. Yan, S. X. Dou and W. Sun, *Adv. Funct. Mater.*, 2017, **27**, 1702317.
2 X.-Y. Yu, L. Yu and X. W. D. Lou, *Adv. Energy Mater.*, 2016, **6**, 1501333.
3 W. Wang, B. Jiang, C. Qian, F. Lv, J. Feng, J. Zhou, K. Wang, C. Yang, Y. Yang and S. Guo, *Adv. Mater.*, 2018, **30**, 1801812.
4 T. Chen, L. Ma, B. Cheng, R. Chen, Y. Hu, G. Zhu, Y. Wang, J. Liang, Z. Tie, J. Liu and Z. Jin, *Nano Energy*, 2017, **38**, 239–248.
5 L. Yu, J. F. Yang and X. W. Lou, *Angew. Chem., Int. Ed.*, 2016, **55**, 13422–13426.
6 H. Hu, Bu Y. Guan and X. W. Lou, *Chem*, 2016, **1**, 102–113.
7 Y. Fang, B. Y. Guan, D. Luan and X. W. D. Lou, *Angew. Chem., Int. Ed. Engl.*, 2019, **58**, 7739–7743.
8 Z. Wei, L. Wang, M. Zhuo, W. Ni, H. Wang and J. Ma, *J. Mater. Chem. A*, 2018, **6**, 12185–12214.
9 H. Li, Y. Su, W. Sun and Y. Wang, *Adv. Funct. Mater.*, 2016, **26**, 8345–8353.
10 N.-S. Choi, Z. Chen, S. A. Freunberger, X. Ji, Y.-K. Sun, K. Amine, G. Yushin, L. F. Nazar, J. Cho and P. G. Bruce, *Angew. Chem., Int. Ed.*, 2012, **51**, 9994–10024.
11 L. Shi, D. Li, P. Yao, J. Yu, C. Li, B. Yang, C. Zhu and J. Xu, *Small*, 2018, **14**, 1802716.
12 J. Wang, D. Chao, J. Liu, L. Li, L. Lai, J. Lin and Z. Shen, *Nano Energy*, 2014, **7**, 151–160.
13 Y. Fang, X. Y. Yu and X. W. D. Lou, *Adv. Mater.*, 2018, **30**, e1706668.
14 X. Zhou, X. Zhu, X. Liu, Y. Xu, Y. Liu, Z. Dai and J. Bao, *J. Phys. Chem. C*, 2014, **118**, 22426–22431.
15 J. Wang, Y. Cui and D. Wang, *Adv. Mater.*, 2019, **31**, e1801993.
16 F. Xie, L. Zhang, C. Ye, M. Jaroniec and S. Z. Qiao, *Adv. Mater.*, 2019, **31**, e1800492.
17 G. Zhou, Y. Zhao and A. Manthiram, *Adv. Energy Mater.*, 2015, **5**, 1402263.
18 L. Zeng, Y. Fang, L. Xu, C. Zheng, M.-Q. Yang, J. He, H. Xue, Q. Qian, M. Wei and Q. Chen, *Nanoscale*, 2019, **11**, 6766–6775.
19 W. J. Yu, C. Liu, L. Zhang, P. X. Hou, F. Li, B. Zhang and H. M. Cheng, *Adv. Sci.*, 2016, **3**, 1600113.
20 Y. Liu, X.-Y. Yu, Y. Fang, X. Zhu, J. Bao, X. Zhou and X. W. Lou, *Joule*, 2018, **2**, 725–735.
21 C. Ye, L. Zhang, C. Guo, D. Li, A. Vasileff, H. Wang and S.-Z. Qiao, *Adv. Funct. Mater.*, 2017, **27**, 1702524.
22 Y. Fang, X. Y. Yu and X. W. D. Lou, *Angew. Chem., Int. Ed.*, 2019, **58**, 7744–7748.
23 X. Zhang, X. Li, J. Liang, Y. Zhu and Y. Qian, *Small*, 2016, **12**, 2484–2491.
24 W. Tang, X. Wang, Y. Zhong, D. Xie, X. Zhang, X. Xia, J. Wu, C. Gu and J. Tu, *Chem.–Eur. J.*, 2018, **24**, 11220–11226.
25 L. Shi and T. Zhao, *J. Mater. Chem. A*, 2017, **5**, 3735–3758.
26 X. Wang, J. Feng, Y. Bai, Q. Zhang and Y. Yin, *Chem. Rev.*, 2016, **116**, 10983–11060.
27 X. Cao, C. Tan, X. Zhang, W. Zhao and H. Zhang, *Adv. Mater.*, 2016, **28**, 6167–6196.
28 S. M. Oh, S. B. Patil, X. Jin and S. J. Hwang, *Chem.–Eur. J.*, 2018, **24**, 4757–4773.
29 Q. Yun, L. Li, Z. Hu, Q. Lu, B. Chen and H. Zhang, *Adv. Mater.*, 2019, 1903826.
30 J. Wang, J. Wan and D. Wang, *Acc. Chem. Res.*, 2019, **52**, 2169–2178.
31 X. Zhao, J. Wang, R. Yu and D. Wang, *J. Am. Chem. Soc.*, 2018, **140**, 17114–17119.
32 H. Yang, S. Huang, X. Huang, F. Fan, W. Liang, X. H. Liu, L. Q. Chen, J. Y. Huang, J. Li, T. Zhu and S. Zhang, *Nano Lett.*, 2012, **12**, 1953–1958.
33 X.-Y. Yu, L. Yu, L. Shen, X. Song, H. Chen and X. W. D. Lou, *Adv. Funct. Mater.*, 2014, **24**, 7440–7446.
34 P. Zhang, B. Y. Guan, L. Yu and X. W. D. Lou, *Angew. Chem., Int. Ed.*, 2017, **56**, 7141–7145.
35 S. N. Tiruneh, B. K. Kang, H. W. Choi, S. B. Kwon, M. S. Kim and D. H. Yoon, *Small*, 2018, **14**, e1802933.
36 Z. Liu, T. Lu, T. Song, X.-Y. Yu, X. W. Lou and U. Paik, *Energy Environ. Sci.*, 2017, **10**, 1576–1580.
37 F. Wang, G. Li, X. Meng, Y. Li, Q. Gao, Y. Xu and W. Cui, *Inorg. Chem. Front.*, 2018, **5**, 2462–2471.
38 C. Wu, Y. Jiang, P. Kopold, P. A. van Aken, J. Maier and Y. Yu, *Adv. Mater.*, 2016, **28**, 7276–7283.
39 W.-J. Yu, C. Liu, L. Zhang, P.-X. Hou, F. Li, B. Zhang and H.-M. Cheng, *Adv. Sci.*, 2016, **3**, 1600113.
40 Y. Xiao, J.-Y. Hwang, I. Belharouak and Y.-K. Sun, *ACS Energy Lett.*, 2017, **2**, 364–372.
41 X. Zhang, R. Zhao, Q. Wu, W. Li, C. Shen, L. Ni, H. Yan, G. Diao and M. Chen, *ACS Nano*, 2017, **11**, 8429–8436.
42 X. Zhang, R. Zhao, Q. Wu, W. Li, C. Shen, L. Ni, H. Yan, G. Diao and M. Chen, *J. Mater. Chem. A*, 2018, **6**, 19004–19012.
43 H. Liu, H. Guo, B. Liu, M. Liang, Z. Lv, K. R. Adair and X. Sun, *Adv. Funct. Mater.*, 2018, **28**, 1707480.
44 M. Yin, X. Feng, D. Zhao, Y. Zhao, H. Li, W. Zhou, H. Liu, X. Bai, H. Wang, C. Feng and Q. Jiao, *ACS Sustainable Chem. Eng.*, 2019, **7**, 6122–6130.
45 W. Zhu, Z. Chen, Y. Pan, R. Dai, Y. Wu, Z. Zhuang, D. Wang, Q. Peng, C. Chen and Y. Li, *Adv. Mater.*, 2019, **31**, e1800426.
46 T. Chen, Z. Zhang, B. Cheng, R. Chen, Y. Hu, L. Ma, G. Zhu, J. Liu and Z. Jin, *J. Am. Chem. Soc.*, 2017, **139**, 12710–12715.

Open Access Article. Published on 26 December 2019. Downloaded on 2/19/2026 12:47:17 PM.
This article is licensed under a Creative Commons Attribution-NonCommercial 3.0 Unported Licence.

47 S. Zhang, G. Wang, Z. Zhang, B. Wang, J. Bai and H. Wang, *Small*, 2019, **15**, e1900565.
48 Z. Chen, R. Wu, M. Liu, H. Wang, H. Xu, Y. Guo, Y. Song, F. Fang, X. Yu and D. Sun, *Adv. Funct. Mater.*, 2017, **27**, 1702046.
49 X. Wu, S. Li, B. Wang, J. Liu and M. Yu, *Phys. Chem. Chem. Phys.*, 2017, **19**, 11554–11562.
50 B. Jia, Q. Yu, Y. Zhao, M. Qin, W. Wang, Z. Liu, C.-Y. Lao, Y. Liu, H. Wu, Z. Zhang and X. Qu, *Adv. Funct. Mater.*, 2018, **28**, 1803409.
51 J. Liu, C. Wu, D. Xiao, P. Kopold, L. Gu, P. A. van Aken, J. Maier and Y. Yu, *Small*, 2016, **12**, 2354–2364.
52 S. D. Seo, D. Park, S. Park and D. W. Kim, *Adv. Funct. Mater.*, 2019, **29**, 1903712.
53 Z. Chen, R. Wu, H. Wang, K. H. L. Zhang, Y. Song, F. Wu, F. Fang and D. Sun, *Nano Res.*, 2017, **11**, 966–978.
54 H. Hu, J. Zhang, B. Guan and X. W. Lou, *Angew. Chem., Int. Ed.*, 2016, **55**, 9514–9518.
55 Z. Deng, H. Jiang, Y. Hu, C. Li, Y. Liu and H. Liu, *AIChE J.*, 2018, **64**, 1965–1974.
56 Y. Yang, M. Luo, Y. Xing, S. Wang, W. Zhang, F. Lv, Y. Li, Y. Zhang, W. Wang and S. Guo, *Adv. Mater.*, 2018, **30**, e1706085.
57 C. Zhu, P. Kopold, W. Li, P. A. van Aken, J. Maier and Y. Yu, *Adv. Sci.*, 2015, **2**, 1500200.
58 Y. Guo, J. Tang, H. Qian, Z. Wang and Y. Yamauchi, *Chem. Mater.*, 2017, **29**, 5566–5573.
59 P. He, Y. Fang, X. Y. Yu and X. W. D. Lou, *Angew. Chem., Int. Ed.*, 2017, **56**, 12202–12205.
60 M. Yi, A. Wu, Q. Chen, D. Cai and H. Zhan, *Chem. Eng. J.*, 2018, **351**, 678–687.
61 G. Yilmaz, K. M. Yam, C. Zhang, H. J. Fan and G. W. Ho, *Adv. Mater.*, 2017, **29**, 1606814.
62 T. Quan, N. Goubard-Bretesché, E. Härk, Z. Kochovski, S. Mei, N. Pinna, M. Ballauff and Y. Lu, *Chem.–Eur. J.*, 2019, **25**, 4757–4766.
63 S. Wang, B. Y. Guan, L. Yu and X. W. D. Lou, *Adv. Mater.*, 2017, **29**, 1702724.
64 L. Wang, X. Zhang, L. Deng, J. Tang, H. Deng, W. Hu and Z. Liu, *ACS Appl. Mater. Interfaces*, 2019, **11**, 4995–5002.
65 Q. Y. B. Jia, Y. Zhao, M. Qin, W. Wang, Z. Liu, C.-Y. Lao, Y. Liu, H. Wu, Z. Zhang and X. Qu, *Adv. Funct. Mater.*, 2018, 1803409.
66 L. Xu, Y. Hu, H. Zhang, H. Jiang and C. Li, *ACS Sustainable Chem. Eng.*, 2016, **4**, 4251–4255.
67 F. Han, C. Y. Jun Tan and Z. Gao, *J. Power Sources*, 2017, **339**, 41–50.
68 K. Wang, Y. Huang, X. Qin, M. Wang, X. Sun and M. Yu, *ChemElectroChem*, 2017, **4**, 2308–2313.
69 Z. Chen, R. Wu, H. Wang, Y. Jiang, L. Jin, Y. Guo, Y. Song, F. Fang and D. Sun, *Chem. Eng. J.*, 2017, **326**, 680–690.
70 J. Ding, H. Zhang, H. Zhou, J. Feng, X. Zheng, C. Zhong, E. Paek, W. Hu and D. Mitlin, *Adv. Mater.*, 2019, **31**, e1900429.
71 R. Wu, D. P. Wang, X. Rui, B. Liu, K. Zhou, A. W. Law, Q. Yan, J. Wei and Z. Chen, *Adv. Mater.*, 2015, **27**, 3038–3044.
72 L. Yu, B. Y. Xia, X. Wang and X. W. Lou, *Adv. Mater.*, 2016, **28**, 92–97.
73 C. Zhu, Y. Wen, P. A. van Aken, J. Maier and Y. Yu, *Adv. Funct. Mater.*, 2015, **25**, 2335–2342.
74 D. Yuan, G. Huang, D. Yin, X. Wang, C. Wang and L. Wang, *ACS Appl. Mater. Interfaces*, 2017, **9**, 18178–18186.
75 Z. Zhang, Y.-P. Deng, Z. Xing, D. Luo, S. Sy, Z. P. Cano, G. Liu, Y. Jiang and Z. Chen, *ACS Nano*, 2019, **13**, 7062–7072.
76 Q. Yun, Q. Lu, X. Zhang, C. Tan and H. Zhang, *Angew. Chem., Int. Ed.*, 2018, **57**, 626–646.
77 F. Tu, X. Xu, P. Wang, L. Si, X. Zhou and J. Bao, *J. Phys. Chem. C*, 2017, **121**, 3261–3269.
78 C. Xu, D. Niu, N. Zheng, H. Yu, J. He and Y. Li, *ACS Sustainable Chem. Eng.*, 2018, **6**, 5999–6007.
79 Q. Cui, Y. Zhong, L. Pan, H. Zhang, Y. Yang, D. Liu, F. Teng, Y. Bando, J. Yao and X. Wang, *Adv. Sci.*, 2018, **5**, 1700902.
80 G. Chen, L. Yan, H. Luo and S. Guo, *Adv. Mater.*, 2016, **28**, 7580–7602.
81 Y. Xu, Y. Wen, Y. Zhu, K. Gaskell, K. A. Cychosz, B. Eichhorn, K. Xu and C. Wang, *Adv. Funct. Mater.*, 2015, **25**, 4312–4320.
82 A. Fu, C. Wang, F. Pei, J. Cui, X. Fang and N. Zheng, *Small*, 2019, **15**, 1804786.
83 Z. W. Seh, J. H. Yu, W. Li, P.-C. Hsu, H. Wang, Y. Sun, H. Yao, Q. Zhang and Y. Cui, *Nat. Commun.*, 2014, **5**, 5017.
84 T. Tang and Y. Hou, *Small Methods*, 2019, 1900001.
85 H. J. Peng, J. Q. Huang, X. Y. Liu, X. B. Cheng, W. T. Xu, C. Z. Zhao, F. Wei and Q. Zhang, *J. Am. Chem. Soc.*, 2017, **139**, 8458–8466.
86 W. Li, H. Yao, K. Yan, G. Zheng, Z. Liang, Y. M. Chiang and Y. Cui, *Nat. Commun.*, 2015, **6**, 7436.
87 J. Liang, X. Li, Y. Zhao, L. V. Goncharova, G. Wang, K. R. Adair, C. Wang, R. Li, Y. Zhu, Y. Qian, L. Zhang, R. Yang, S. Lu and X. Sun, *Adv. Mater.*, 2018, **30**, e1804684.
88 Y. Fang, X.-Y. Yu and X. W. Lou, *Matter*, 2019, **1**, 90–114.
89 S. Wang, Y. Fang, X. Wang and X. W. Lou, *Angew. Chem.*, 2019, **131**, 770–773.
90 Z. Hu, Q. Liu, S. L. Chou and S. X. Dou, *Adv. Mater.*, 2017, **29**, 1700606.
91 F. Li, Z. Wei, A. Manthiram, Y. Feng, J. Ma and L. Mai, *J. Mater. Chem. A*, 2019, **7**, 9406–9431.
92 L. Hu, X. Zhu, Y. Du, Y. Li, X. Zhou and J. Bao, *Chem. Mater.*, 2015, **27**, 8138–8145.
93 Y. Du, X. Zhu, X. Zhou, L. Hu, Z. Dai and J. Bao, *J. Mater. Chem. A*, 2015, **3**, 6787–6791.
94 Y. Du, X. Zhu, L. Si, Y. Li, X. Zhou and J. Bao, *J. Phys. Chem. C*, 2015, **119**, 15874–15881.
95 L. Hou, H. Hua, R. Bao, Z. Chen, C. Yang, S. Zhu, G. Pang, L. Tong, C. Yuan and X. Zhang, *ChemPlusChem*, 2016, **81**, 557–563.
96 L. Hou, Y. Shi, C. Wu, Y. Zhang, Y. Ma, X. Sun, J. Sun, X. Zhang and C. Yuan, *Adv. Funct. Mater.*, 2018, **28**, 1705921.
97 Y. Wu, S. Hu, R. Xu, J. Wang, Z. Peng, Q. Zhang and Y. Yu, *Nano Lett.*, 2019, **19**, 1351–1358.